

Neutrinos via Charm Decays in Astrophysical Sources

by

Fritz Ali Agildere

fritz.agildere@udo.edu

2024

THESIS IN PARTIAL FULFILLMENT OF THE
REQUIREMENTS FOR THE DEGREE OF
BACHELOR OF SCIENCE

SUBMITTED TO THE
CHAIR FOR EXPERIMENTAL ASTROPARTICLE PHYSICS
DEPARTMENT OF PHYSICS
TECHNICAL UNIVERSITY OF DORTMUND

EXTERNAL SUPERVISION AT THE
CHAIR FOR THEORETICAL PLASMA ASTROPARTICLE PHYSICS
FACULTY OF PHYSICS AND ASTRONOMY
RUHR UNIVERSITY BOCHUM

First advisor: P.D. Dr. Dominik Elsässer (*Technical University of Dortmund*)
Second advisor: Prof. Dr. Julia Tjus (*Ruhr University Bochum*)
Submission date: July 25, 2024

Zusammenfassung

Platzhalter

Abstract

Placeholder

Acknowledgements

Contents

1	Introduction	1
2	Background	3
2.1	Particle Physics	3
2.1.1	Fundamental Interactions	3
2.1.2	Hadrons & Leptons	4
2.1.3	Reference Frames	5
2.1.4	Particle Collisions	5
2.1.5	Cooling & Decay	5
2.2	Multimessenger Astronomy	7
2.2.1	Magnetic Field Scales	7
2.2.2	High Energy Cutoff	7
2.2.3	Stochastic Acceleration	8
2.2.4	Cosmic Rays	9
2.2.5	Neutrinos	10
2.2.6	Photons	10
2.2.7	Gravitational Waves	10
2.3	Astrophysical Sources	11
2.3.1	Magnetars	11
2.3.2	Spindown	12
2.3.3	Active Galactic Nuclei	13
2.3.4	Accretion Disks	14
3	Methods	16
3.1	Cross Sections	16
3.1.1	Scattering	16
3.1.2	Production	18
3.2	Spectral Distributions	21
3.2.1	Charm	21
3.2.2	Pions & Kaons	22
3.3	Computation	23
3.3.1	Injection	23
3.3.2	Production & Decay	24
3.3.3	Implementation	25
3.3.4	Event Generators	26
4	Results	27
5	Conclusion & Outlook	39
	Bibliography	40

Figures

1	Inelastic cross sections σ_{hp} for hadron-proton scattering.	18
2	Weighted energy cross sections for $pp \rightarrow D^0 X$ production.	20
3	Filtered SIBYLL 2.3c yields from pp at $\sqrt{s} = 1$ TeV energies.	26
4	Magnetar ν flux from c decay including optical depth.	28
5	Magnetar ν flux compared to c decay with optical depth.	29
6	Magnetar ν fluence compared to c decay with optical depth.	30
7	Magnetar ν flux from c decay excluding optical depth.	32
8	Magnetar ν flux compared to c decay without optical depth.	33
9	Magnetar ν fluence compared to c decay without optical depth.	34
10	AGN accretion disk ν fluence from c decay.	37
11	AGN accretion disk ν fluence compared to c decay.	38

Tables

1	Fits to the total cross sections σ_{hp} in hadron-proton collisions.	17
2	Ratio of model-independent elastic and total σ_{hp} cross sections.	17
3	Parametrization of the c quark differential cross section.	19
4	Coefficients for c hadron production, cooling and decay.	22
5	Parametrized spectral distribution for π production.	22

Abbreviations

AGN	Active Galactic Nucleus
CMB	Cosmic Microwave Background
DSA	Diffusive Shock Acceleration
EW	Electroweak Theory
FF	Fragmentation Function
GR	General Relativity
GZK	Greisen-Zatsepin-Kuzmin
PDF	Parton Distribution Function
QCD	Quantum Chromodynamics
QED	Quantum Electrodynamics
QFT	Quantum Field Theory
QM	Quantum Mechanics
SM	Standard Model
SMBH	Super-Massive Black Hole
SR	Special Relativity
UHECR	Ultra-High-Energy Cosmic Ray

1 Introduction

In their quest for a deeper understanding of astrophysical phenomena, researchers have moved to investigating a combination of different signal types. This has given rise to the independent field of multimessenger astronomy that studies electromagnetic radiation, cosmic rays, neutrinos and gravitational waves to infer which processes drive their sources [1]. While such environments are likely opaque to photons, charged particles may escape after being accelerated, creating a non-thermal *Ultra-High-Energy Cosmic Ray* (UHECR) population [2]. Experiments do indeed support this expectation by regular measurements of energies from 10^9 GeV up to 10^{11} GeV in accordance with the *Greisen-Zatsepin-Kuzmin* (GZK) cutoff [3]. The question then becomes if it is possible to reconstruct any source region properties from these signals.

One basic constraint derived from observations of extreme energies is a relationship between the sizes and field strengths of possible sources [4]. From this follows that plausible candidates for UHECR origins consist mostly of extragalactic regions like *Active Galactic Nuclei* (AGN) that are powered by *Super-Massive Black Hole* (SMBH) engines at their center, as well as more exotic scenarios involving stellar remnants such as white dwarfs or neutron stars [5–7]. Matching cosmic ray signals to their sources, however, proves to be an extremely difficult task, as large scale turbulent magnetic fields isotropize the arrival directions of charged messenger particles.

This leaves neutrinos and gravitational waves as multimessenger candidates, both of which are the subjects of multiple promising discoveries at high-energy detection facilities [8–10]. Although gravitational signals provide valuable insights regarding the interaction and structure of massive objects, they do not carry much information on particle acceleration. Astrophysical neutrinos, on the other hand, are produced in hadronic reactions with proton or photon fields close to the accelerating regions. Their weakly interacting nature allows them to escape and propagate almost freely, making them reliable pointers to their sources [2].

Due to this strong physical connection between highly energetic neutrinos and hadronic cosmic rays, they are thought to have closely related origins. Recent combined analyses indicating simultaneous neutrino and gamma emissions from a flaring blazar seem to be in agreement with this assumption for the case of an AGN scenario [11, 12]. More compact sources such as strongly magnetized pulsars are also an area that is being actively researched [13]. The standard approach to modeling these sites starts with injecting protons accelerated by some astrophysical process into a photonic or baryonic target surrounding the potential source. In the resulting interactions, energetic pions and kaons are produced, which then decay to neutrinos. This method is generally self-consistent and capable of producing plausible results, but neglects certain effects that might reveal more detailed information about the respective source [14].

1 Introduction

When working towards describing sources of neutrinos in the upper UHECR energy ranges, intermediate hadrons must exhibit highly relativistic velocities. Accordingly, these particles experience extreme time dilation, leading to lifetimes appearing several orders of magnitude longer than in their rest frames when viewed from the surrounding fields. If sufficiently high matter densities are present, the typically investigated pions and kaons are therefore inelastically scattered to lower energies before decaying to neutrinos. Due to their much shorter lifetimes, more exotic particles then become significant contributors to the total neutrino flux that would otherwise remain suppressed. Of this population, hadrons containing at least one charm quark are expected to be most dominant at typical UHECR energies [15].

The present thesis estimates the relative neutrino contribution from decays of such charmed hadrons. For this purpose, results of the magnetar case presented in [14] are reproduced before applying the same procedure to a simplified AGN accretion disk model, assessing the feasibility of charm decay dominance in this latter scenario.

Following this introduction, Chapter 2 summarizes the core physical concepts relevant to this thesis, including particle physics, multimessenger astronomy, and their connection to the treated astrophysical sources. Based on this background, Chapter 3 introduces semianalytical methods involving empirical parametrizations, which are then employed for all further computations. Lastly, Chapter 4 presents the results, with Chapter 5 providing a concluding discussion as well as potential future prospects based on these findings.

On the topic of unit conventions, this thesis uses varying styles for different contexts. Physical equations are usually given in Gaussian units, while masses might have natural units of energy when concerning particle physics or be written as multiples of the solar mass in astrophysical settings. The latter context also uses parsecs as measurements of very large distances. To avoid ambiguities, units will be clarified in the text whenever necessary.

2 Background

On their journey through space, messenger particles are subject to various influences, both in terms of type and scale, before reaching our planet. Understanding this propagation requires a thorough description of different physical processes at all scales of application, from production in astrophysical sources, through interactions with the radiation and matter fields that fill the cosmos, to entering the solar system and ultimately the terrestrial atmosphere. The following sections provide an overview of aspects relevant to the treatment of this complex topic, as well as references for further study on the various related subjects.

2.1 Particle Physics

In our modern view, interactions and categories of elementary particles are most accurately described by a construct called the *Standard Model* (SM) of particle physics. Underlying this formalism is the mathematical framework known as *Quantum Field Theory* (QFT) that combines and generalizes properties of *Quantum Mechanics* (QM) and *Special Relativity* (SR) to produce a consistent description of microscopic reality. Excitations in the associated fields are referred to as quanta and manifest themselves as observable particles [16]. Since this thesis is mostly concerned with the statistical behaviors of large quantities instead of individual particle probabilities, a more detailed treatment is omitted, with the exception of certain phenomena important to the justification of some later assumptions.

2.1.1 Fundamental Interactions

With the theory of *Quantum Electrodynamics* (QED) representing a quantized description of classical electromagnetism, the first successful QFT formulation had been realized. It governs all interactions between electrical charges that involve photons and predicts observations with extremely high precision. Each subsequent QFT is built on a foundation of QED achievements, such as *Quantum Chromodynamics* (QCD) for strong force interactions or the unified framework of *Electroweak Theory* (EWT) that includes both weak force and electromagnetic phenomena.

According to the SM formalism, these interactions are mediated by bosonic elementary particles, namely massless photons γ for electrodynamics or gluons g in case of the strong force sector, as well as massive Z and W^\pm bosons that carry the weak force. The only remaining fundamental interaction not contained in the SM is gravity, the effects of which are currently best described in terms of *General Relativity* (GR) as the continuous macroscopic curvature of spacetime due to the presence of large masses. Because elementary particles exclusively inhabit microscopic scales, their behavior is usually indistinguishable from that described by SR in flat space [16].

2.1.2 Hadrons & Leptons

In addition to the previously listed gauge bosons, the SM further includes elementary fermions as the fundamental constituents of matter. These sort into the categories of quarks and leptons, both of which are further grouped by generations of quark or lepton pairs. Ordered according to their generation, there are flavors of up and down, charm and strange, as well as top and bottom for quarks, which are denoted by their initial letters. For charged leptons, there exist electrons e as well as the heavier muon μ and tau τ that each have an associated neutrino ν_l with no electrical charge. This picture is completed by the corresponding antiquarks and antileptons for all particles mentioned above [17].

Apart from an electrical charge, quarks are also carriers of so-called color charges that couple to gluons, which, in contrast to the electrically neutral photons, carry colors themselves. Gluons are therefore capable of self-coupling, leading to higher binding energies with increasing distances. If removed far enough, this energy is eventually released by producing a quark pair, ultimately leading to the creation of bound color-neutral states.

These resulting composite particles are called hadrons, with the entire process being referred to as hadronization. This naturally leads to the concept of confinement, which states that quarks cannot exist as free particles, with the notable exception of very high energies. In these regimes, strong force coupling becomes small and allows quarks to behave almost freely, defining the term asymptotic freedom. A major consequence of this is that perturbative QCD calculations become possible, which would otherwise require complex approaches such as discrete QCD on a lattice or some type of effective field theory instead [18].

The quark model enables classification of hadrons based on their constituent numbers. Baryons are comprised of three quarks, all with different colors, while mesons contain two quarks with opposite color and anticolor charges. From the spin algebra, baryons clearly obey fermionic statistics, while mesons act as bosons. Exemplary quark contents are given for baryons such as protons $p \equiv uud$ and neutrons $n \equiv udd$ as well as pions $\pi^- \equiv \bar{u}d$ and kaons $K^- \equiv \bar{u}s$ in the case of mesons. The charmed hadrons considered in this thesis are the same mesons $D^0 \equiv c\bar{u}$ as well as $D^- \equiv \bar{c}d$ and $D_s^- \equiv \bar{c}s$ with the baryon $\Lambda_c^+ \equiv udc$ as in [14]. Specific decay channels will be listed directly in the relevant sections with [19] providing a broad overview.

Contrary to hadrons, leptons are fundamental particles. Due to being colorless, they are not affected by the strong force, meaning that all leptonic interactions obey EWT instead. Noting that photons only couple to electrical charges, this leaves neutrinos as the only particles which interact exclusively via the weak force. Here, one distinctive feature of the weak interaction should be mentioned as well, namely that of parity violation. This manifests by only coupling to left-handed components of particles and right-handed components of antiparticles. Handedness in this context refers to chirality, which for massless particles is equivalent to helicity or the sign of the spin projection onto the momentum vector. Because the SM assigns zero mass to neutrinos, this EWT property suppresses certain decay modes and enforces correlated polarizations for the involved leptons. Not included in the SM is the observation of neutrino oscillations, which are, however, not relevant for this thesis, since flavor differences are neglected [16].

2.1.3 Reference Frames

Depending on the application, energies in particle physics are either given as viewed from a suitable rest frame or independent from the choice of coordinates altogether. One particularly convenient formulation uses incoming and outgoing momenta p_1, p_2 and p_3, p_4 to define

$$s = (p_1 + p_2)^2, \quad t = (p_1 - p_3)^2, \quad u = (p_1 - p_4)^2$$

as the Mandelstam variables s, t, u , which assign different channels to scattering processes based on the squared momentum carried by an exchanged mediating particle. Implied in this context is a Minkowski inner product, making the above quantities manifestly Lorentz invariant. When working with parametrizations defined for use in different subdisciplines, it regularly becomes necessary to convert from center of mass energies \sqrt{s} given by the square root of the Mandelstam s to the energy E of a projectile as viewed in the system of a stationary target, where vectors $P = (E, \mathbf{P}c)$ and $p = (mc^2, 0)$ represent the respective particle momenta. With a classical projectile momentum \mathbf{P} and c denoting the speed of light, rest masses M and m for projectile and target lead to $E^2 = \mathbf{P}^2 c^2 + M^2 c^4$ as well as

$$s = (P + p)^2 = (E + mc^2)^2 - \mathbf{P}^2 c^2 = 2Emc^2 + m^2 c^4 + M^2 c^4,$$

which is also referred to as the invariant mass. The trailing terms in this equation are negligible at high energies, allowing for an approximation $s = 2Emc^2$ in the target rest frame.

2.1.4 Particle Collisions

Another important aspect of particle physics is the description of collision processes. For this purpose, the concept of cross sections σ should be understood. In classical mechanics, these quantities are solely related to geometric properties of the objects involved, assuming they only interact upon impact. If longer range forces are included, the cross section represents a larger effective area that measures how the trajectory of an incoming projectile is influenced by the target. Additionally, differential cross sections with respect to some independent variable such as solid angle $d\sigma/d\Omega$ or kinetic energy $d\sigma/dE$ can be defined. Measurements of this quantity often reveal more information about the inner structure of targets. To distinguish these cases, one might refer to σ as the integrated cross section. Since QM is at the core of particle physics, cross sections in this context are instead interpreted as probability measures of fundamentally stochastic collision processes, such as the production of specific particles. It can also be useful to separate cross sections into elastic and inelastic components, especially for collisions in which particles lose energy, as is the case for cooling processes via scattering.

2.1.5 Cooling & Decay

Consider an infinitesimally thin slice of a target medium with particle number density n and volume $V = Sdx$ where S and dx measure surface area and thickness, respectively. Accordingly, there exist $\tilde{N} = nV$ targets that each have effective interaction cross sections $\tilde{\sigma}$ with a total coverage of $\tilde{S} = \tilde{\sigma}\tilde{N}$ as viewed by an incident projectile.

Probabilities for dissipating the beam constituent energy are then given by the ratio $\mathcal{P} = \tilde{S}/S$ of both areas or explicitly $\mathcal{P} = \tilde{\sigma} n dx$ in case of dx as the covered distance. Expressing $\tilde{\sigma} = \kappa \sigma$ in terms of the inelastic scattering cross section σ and a dimensionless factor κ called inelasticity, one can identify a length scale $\lambda = (\kappa \sigma n)^{-1}$ as the mean free path between collisions. Multiplying with κ includes the ratio of remaining to initial energy, which is taken to be constant. From this follows a reduction in beam particles $dN = -N \lambda^{-1} dx$ proportional to N as the total projectile count and $\mathcal{P} = \lambda^{-1} dx$ for the reformulated probability which represents an ordinary differential equation of first order. The solution is found to follow an exponential law

$$N(x) = N_0 \exp\left(-\frac{x}{\lambda}\right)$$

where N particles remain over some distance x with N_0 as the initial amount. Furthermore,

$$P(x) = 1 - \exp\left(-\frac{x}{\lambda}\right)$$

gives the probability of a particle having been scattered after travelling x length units. Similar steps for time instead of distance lead to the well known equation

$$N(t) = N_0 \exp\left(-\frac{t}{\tau}\right)$$

describing exponential decay. It commonly appears in the context of radioactive materials but also applies to hadrons and leptons or more generally any quantity which decreases at a rate proportional to itself. Analogous to the previous case, a particle decays with probability

$$P(t) = 1 - \exp\left(-\frac{t}{\tau}\right)$$

before a time t has passed and for τ as the mean lifetime. Translating this from rest frame to laboratory coordinates defines the decay timescale $t_{\text{dec}} = \tau \Gamma$ with a Lorentz factor $\Gamma = E/m$ via projectile energy and invariant mass. This is equivalent to a characteristic decay length given by $\lambda_{\text{dec}} = v t_{\text{dec}}$ where the velocity $v = c$ can be set for highly relativistic particles. Additionally, mean free path and cooling distance $\lambda_{\text{cool}} = (\kappa \sigma n)^{-1}$ refer to exchangeable concepts. Particles lose energy in every collision, which is the same as reducing temperature from a thermodynamics perspective. Dividing by the speed of light c translates this expression to $t_{\text{cool}} = (\kappa \sigma n c)^{-1}$ as a cooling timescale. Analogously, the distance $\lambda_{\text{dec}} = c \tau E/m$ can be rewritten as $t_{\text{dec}} = \tau E/m$ in units of time. Substituting into the decay formula yields a cooling factor

$$C = 1 - \exp\left(-\frac{t_{\text{cool}}}{t_{\text{dec}}}\right) \quad (1)$$

that rescales spectra from direct production to account for decay processes taking place after collisional energy losses have occurred. This is an essential mechanism for the hypothesis that neutrinos from charm dominate pion and kaon contributions at high energies. While longer lived particles experience significant cooling thanks to time dilation, charmed hadrons decay promptly in comparison, resulting in a neutrino flux that directly traces the underlying hadronic population. One requirement for the validity of (1) is that $\lambda_{\text{dec}} \ll d$ holds, with d measuring the target field size to ensure decays occur exclusively inside this region.

Another quantity relevant to the context at hand is an optical depth $\mathcal{O} = d/\lambda$ that represents the distance d to mean free path λ ratio. Inserting its definition yields a factor

$$\mathcal{O} = \kappa \sigma n d, \quad (2)$$

which is used as a first order multiplicative modification to account for attenuation effects on the spectra. This can be understood by considering that higher target medium densities and larger scattering cross sections over longer distances lead to more interactions with the projectile.

2.2 Multimessenger Astronomy

A recent extension of traditional astronomy, the field of multimessenger astrophysics continues to evolve whilst providing otherwise inaccessible insights via the combination of complementary information carried by multiple messenger species. This section begins by expanding on physical concepts alluded to in Chapter 1 before continuing to describe the available multimessenger candidates in some detail. For a more extensive overview, refer to [1].

2.2.1 Magnetic Field Scales

Particles carrying electrical charges $Q = Ze$ in orthogonal motion at velocity v to a homogenous magnetic field B are acted on by the Lorentz force $F = QvB$ that produces a gyrating motion. With the elementary charge e and Γ as a Lorentz factor, this must balance a relativistic centripetal force $F = m\Gamma v^2/R$ with Larmor radius R on the resulting circular path. Rearranging variables and identifying $p = m\Gamma v$ leads to the solution

$$R = \frac{p}{QB}$$

on which the magnetic field extent D imposes $R < D$ as a condition. In case of highly relativistic energies, one can substitute $E = pc$ for the momentum to obtain an inequality $E < QcBD$ from the above considerations. Realistic astrophysical magnetic fields are not ordered, instead following turbulences that travel through the plasma. To include the effects of moving scattering centers, a factor β proportional to the Alfvén velocity is included, giving

$$E < Ze\beta cBD$$

as the Hillas criterion. It is named after its description in [4] and connects source region sizes to the strength of prevailing magnetic fields, with observed cosmic ray energies as a constraint.

2.2.2 High Energy Cutoff

At very high energies, protons and nuclei interact with cosmic photons, which can be blueshifted up to extreme gamma regimes due to the Doppler effect. In these processes, the photon spin is absorbed to produce a delta resonance Δ^+ representing an excited proton state.

This decays almost immediately to pairs of nucleons and pions, leading to probable reaction channels $p\gamma \rightarrow n\pi^+$ or $p\gamma \rightarrow p\pi^0$ and resulting in an altered particle momentum. For the case of *Cosmic Microwave Background* (CMB) radiation, a close to perfect black body spectrum

$$\frac{dn}{d\epsilon}(\epsilon) = \frac{\epsilon^2}{\pi^2 \hbar^3 c^3 (e^{\epsilon/k_B T} - 1)}$$

is given by [20] as the number density. From CMB temperatures of $T = 2.725$ K follows that significant photon numbers exist with energies around $\epsilon = 10^{-12}$ GeV in the CMB rest frame. To find a threshold in center of mass coordinates, the scalar product is used for

$$s = (p_p + p_\gamma)^2 = p_p^2 + p_\gamma^2 + 2p_p p_\gamma = m_p^2 c^4 + 2E\epsilon = M^2 c^4,$$

where $M = m_p + m_\pi$ and $m_\gamma = 0$ as well as head-on collisions have been assumed. The solution

$$E = ((m_p + m_\pi)^2 c^4 - m_p^2 c^4) / (2\epsilon)$$

corresponds to roughly $E = 10^{11}$ GeV for the so-called GZK cutoff. Energies that exceed this value when viewed from CMB coordinates lead to significant losses, making the universe opaque to such protons. If pair production $\gamma \rightarrow e^+ e^-$ from proton interactions is considered, one finds

$$E = ((m_p + 2m_e)^2 c^4 - m_p^2 c^4) / (2\epsilon)$$

or approximately $E = 10^9$ GeV by setting $M = m_p + 2m_e$ instead. Similar constraints apply when considering alpha particles and heavier nuclei, while electrons are limited mainly by Compton down-scattering. Additionally, there exist infrared and radio backgrounds as potentially relevant radiation fields. From the multiple competing mechanisms for energy losses and momentum isotropization, it is as a consequence extremely challenging to reliably interpret cosmic ray signals and practically impossible to reconstruct any information about specific sources.

2.2.3 Stochastic Acceleration

From the introduction of theoretical limits in Sections 2.2.1 and 2.2.2 arises the question of how particles reach these high energy regimes in the first place. Due to its relatively simple derivation and surprising accuracy in the description of measured spectra, probabilistic collisions are often viewed as one of the most plausible mechanisms responsible for cosmic ray acceleration. The general case is described in [21] and supposes that for each collision, particles gain some energy proportional to a constant factor η and remain in the accelerating region with probability ς on average. With initial conditions N_0 for the number of particles and E_0 as the mean energy, this results in $N = N_0 \varsigma^k$ and $E = E_0 \eta^k$ after k collisions. Using $\ln x^k = k \ln x$ in

$$\frac{\ln(N/N_0)}{\ln(E/E_0)} = \frac{\ln(\varsigma)}{\ln(\eta)}$$

eliminates the exponent and allows terms to be rearranged to solve for the desired quantity.

From this follows a connection between energy and number of particles

$$N = N_0 \left(\frac{E}{E_0} \right)^{\ln(\zeta)/\ln(\eta)}$$

that incidentally obeys a power law, which is an almost ubiquitous feature observed in cosmic ray physics. One can interpret the above expression as an integrated spectrum, leading to

$$\frac{dN}{dE} = \frac{N_0}{E_0} \left(\frac{E}{E_0} \right)^\alpha$$

for the differential case with a characteristic spectral index

$$\alpha = \frac{\ln(\zeta)}{\ln(\eta)} - 1$$

constrained by $\ln(\zeta)/\ln(\eta) < 0$ due to $\zeta < 1$ and $\eta > 1$ as implied per the definitions.

The basic case of *Diffusive Shock Acceleration* (DSA) considers shock fronts that propagate with velocity $\beta = v/c$ in a fully ionized gas. Requiring momentum isotropization without significant energy losses on each side of the discontinuity results in $\ln(\zeta)/\ln(\eta) = -1$ and a corresponding spectral dependence $dN/dE \propto E^{-2}$ that is discussed by [21] as well. A slightly steeper index around $\alpha = -2.5$ can be derived when nonlinear effects are accounted for.

Energy gain increasing linearly with β leads to this mechanism being categorized as first order Fermi acceleration, whereas the originally proposed formulation scales like β^2 or as second order. Though shocks exceed the local speed of sound in the astrophysical medium, relativistic velocities are typically not achieved. Consequently, ratios of $\beta \ll 1$ mean that lower order processes are much more efficient in reaching high particle energies.

2.2.4 Cosmic Rays

Consisting of charged particles with strictly non-thermal origins, cosmic rays were first detected at high altitudes over a century ago. Since then, they have become a foundational piece in our understanding of astrophysical sources. Although their flux is dominated by protons, other nuclei as heavy as lead can contribute significant portions at high energies as well. Besides this baryonic component, there are also charged leptons adding to the total population. The exact ratios of these constituents contain information about source compositions, though any reconstruction of individual sources is likely impossible. This is a result of cosmic magnetic fields that scramble the directions of charged particles, leading to a largely isotropic distribution. At the same time, it is possible to constrain the size and field parameters of sources based on the energy of cosmic rays. For this purpose, Section 2.2.1 provides the so-called Hillas condition. In combination with the characteristic broken power law spectrum, one concludes that most cosmic rays are of galactic origin, except for the highest energies, which require extragalactic sources [5, 7]. Beyond these ranges, there appears to be a sharp drop that agrees well with Section 2.2.2 in the case of a GZK cutoff. Both the spectral shape and the extreme energies are also consistent with a modified DSA scenario as described in Section 2.2.3 for cosmic rays [2].

2.2.5 Neutrinos

Their weakly interacting nature introduced in Section 2.1.2 is precisely what makes neutrinos so interesting. After being produced, they penetrate most obstacles that would be completely opaque to any other messenger particle. This comes at the cost of being notoriously difficult to detect, of course, but opens up the opportunity of measuring otherwise inaccessible processes occurring deep inside astrophysical sources. Several different populations are either known or hypothesized, for example those of solar origin, neutrinos from core-collapse supernovae, stellar remnants or active galaxies that are discussed in this thesis, as well as neutrinos from pion decay implied in Section 2.2.2 after GZK photodissociation. Additionally, a primordial neutrino background is expected to exist with a history analogous to that of CMB formation, in which photons decoupled from matter during the recombination epoch [2]. All of these astrophysical and cosmological prospects as well as the previously mentioned flavor oscillations make neutrino astronomy a promising field of research [1].

2.2.6 Photons

With visual observations being conducted for millennia, photonic signals undoubtedly form the most ancient type of astronomy. Advances in optical instrumentation have driven revolutionary progress over the last centuries, culminating in modern detectors unlocking wavelengths across the entire electromagnetic spectrum. Especially radio and gamma frequencies have the potential of contributing to multimessenger astrophysics, with radio waves having the ability to resolve regions obscured by dust, and gamma photons being closely associated with hadronic processes in a similar manner as neutrinos, for instance. Fundamental limitations of astrophysical photon signals consist of a cutoff at very high energies from pair production with CMB photons similar to Section 2.2.2 for protons and nuclei, as well as a gamma ray horizon referring to the impedance caused by interactions with extragalactic background light [22]. Detection is further constrained by the atmospheric window, which is not transparent for all electromagnetic wavelengths.

2.2.7 Gravitational Waves

Setting aside the possibility of gravitons as hypothetical mediating particles, gravitation seems to be a fundamentally continuous phenomenon, in the same way as classical theories like that of electromagnetism by Maxwell. According to Einstein, masses lead to distortions of spacetime that propagate at the speed of light. From this perspective, it readily follows that especially massive systems such as black hole or neutron star binaries emit gravitational waves through their movement. These excitations have an advantage compared to other messengers in that they experience essentially no absorption or scattering by matter. Alongside unimpeded insights into highly energetic merger events, there should also exist a gravitational background radiation containing information about the very early universe.

2.3 Astrophysical Sources

The picture of particle physics building up to multimessenger astronomy will now be realized in the context of plausible astrophysical neutrino sources [2]. In the following section, scenarios for a magnetar as well as an AGN accretion disk are developed.

2.3.1 Magnetars

Neutron stars are stable remnants of massive stellar progenitors that are destroyed in violent core-collapse supernovae after having depleted their fuel reserves. Instead of nuclear fusion, the remaining neutron star is supported against further gravitational contraction by degeneracy pressures. These result from the Pauli exclusion principle that prevents fermions from occupying identical quantum states. While white dwarfs rely primarily on electrons for this mechanism, neutron stars depend on the repulsion among nucleons, placing them among the most dense macroscopic objects in the universe. Due to angular momentum of the progenitor star being conserved in the remnant, the compression of stellar material immediately before a supernova explosion leads to extremely fast rotational periods. In addition to that, conservation of magnetic energy implies large magnetizations as well. The authors in [23] discuss this so-called fossil field hypothesis, but argue that strong convective flows during formation or inside the very young neutron star are more likely culprits. These would also eliminate any prior correlation between the axis of rotation and the field orientation. Because neutron star interiors are assumed to be superconducting fluids, dynamo effects can amplify and sustain any initial magnetic fields [24]. If such a magnetized rotator emits misaligned radio jets, their sweeping motion will be observed as a pulsating radio source, hence the name pulsar. In case of extreme magnetic fields, the respective neutron star is further classified as a magnetar. The decay of these fields is generally modeled as exponential or according to a power law, but can be approximated as being static for the shorter timescales relevant to the present thesis [25]. Surrounding newborn neutron stars are clouds of ejected material, which serve as target fields. Modeling this to be a spherical region of homogeneously distributed matter at each time t after formation of the remnant leads to a number density corresponding to the ratio

$$n_{\text{ej}} = 3M_{\text{ej}} / (4\pi r_{\text{ej}}^3 m_p) \quad (3)$$

for all ejecta mass M_{ej} consisting of protons with m_p masses. By asserting a radial expansion at constant β_{ej} velocities, one finds the ejecta radius

$$r_{\text{ej}} = \beta_{\text{ej}} ct \quad (4)$$

as a function of time. Inside this plasma, free charge carriers weaken the otherwise strong fields, allowing synchrotron losses to be neglected [14]. In vacuo, these would significantly reduce the energy of injected protons, thereby preventing production of highly energetic hadrons and neutrinos. Furthermore, typical densities listed in Section 3.1.2 are sufficiently low for neutrino attenuation effects to be neglected, and a comparison of the optical depth (2) for protons and photons shows that thermal radiation fields are unlikely to influence the overall results [14].

2.3.2 Spindown

To explain observations of rapidly spinning neutron stars or pulsars, there has to exist some mechanism by which rotational energy is lost. Reference [26] gives a brief overview of possible radiation candidates such as gravitational quadrupole or higher order electromagnetic moments. Because this thesis is limited in its scope and concerns itself with the acceleration of electric charges, a pure magnetic dipole approach will be adopted. For more compact and convenient notation, Gaussian units are used.

An idealized view like in [27] models stars as sharply bound and uniformly magnetized spheres, leading to $\mu = R_{\text{ns}}^3 B_{\text{ns}}/2$ for the external magnetic moment [28]. Parameters R_{ns} and B_{ns} measure stellar radius and polar magnetic flux density, respectively. For a rotating dipole in vacuo,

$$L = \frac{2\mu^2\omega^4\sin^2\chi}{3c^3} \quad (5)$$

is the exact expression for radiant power derived in [28] as a standard reference, where a static angle χ between the dipole field and rotational axis with angular frequency ω is assumed. If a force-free limit is applied instead, variational calculations [29] and simulations [30] indicate

$$L = \frac{\mu^2\omega^4(1+\sin^2\chi)}{c^3} \quad (6)$$

as an appropriate expression of the luminosity. This is more accurate than the previous result, as it has been shown by [31] that the surroundings of a neutron star cannot support a vacuum but must instead be filled with a plasma of charge carriers originating from instabilities at the surface. However, one quickly encounters the problem that $\mathbf{E} \cdot \mathbf{B} = 0$ as a condition of force-free magnetospheres prevents particle acceleration. This can be overcome by introducing deviations from such global solutions on local scales as discussed in [32] and [33].

Spindown follows an exponential energy decay $E = E_0 \exp(-t/t_{\text{sd}})$ with the time derivative

$$\dot{E} = -E/t_{\text{sd}} \quad (7)$$

and t_{sd} as a characteristic timescale. Assuming exclusively rotational energy

$$E = I\omega^2/2, \quad (8)$$

where I gives the neutron star moment of inertia, leads to

$$\dot{E} = I\omega\dot{\omega} \quad (9)$$

as an equally valid expression of the energy loss rate. Equations (5) and (6) can be generalized via $L = K\omega^4$ by using a coefficient K containing all information except the dipolar ω^4 dependence.

Identifying this with (7) through $\dot{E} = -L$ and evaluating at $t = 0$ yields $L_0 = K\omega_0^4$ as well as the decay rate $\dot{E}_0 = -I\omega_0^2/2t_{\text{sd}}$ from inserting (8) as the energy, which can be combined to find

$$t_{\text{sd}} = I/2K\omega_0^2$$

for the spindown time. It further follows from equating (9) to the luminosity at any t that

$$I\dot{\omega} = -K\omega^3$$

must hold. This represents a special case of the power law differential equation $\dot{\omega} \propto \omega^n$ with a so-called braking index $n = 3$ typical of a rotating magnetic dipole. As a comparison, one would find $n = 5$ in case of a quadrupole, indicating that n is characteristic of the specific energy loss mechanism involved [26]. After separating variables and integrating, one obtains

$$\omega = \omega_0(1 + t/t_{\text{sd}})^{-1/2}$$

for the frequency as a function of time and spindown scale.

Another important concept for the description of neutron star environments is the so-called light cylinder. It represents the boundary beyond which magnetic field lines can no longer corotate with the central body without exceeding the speed of light, defining $R_{\text{lc}} = c/\omega$ as its radius. Due to the resulting lag, magnetic fields are open, providing a potential mechanism for the acceleration of particles to high energies [31].

With an open field magnetic flux $\psi = \mu/R_{\text{lc}}$ follows $\phi = \psi/R_{\text{lc}}$ as the difference in potential energy. From this, a charge e reaches energies $E^M = \eta e\phi$ with an efficiency $\eta < 1$ limiting the acceleration. Expanding these terms and including the dependence on time,

$$E^M(t) = \frac{\eta e B R^3 \omega_0^2}{2c^2(1 + t/t_{\text{sd}})} \quad (10)$$

states this explicitly. The superscript M denotes a monochromatic energy distribution.

2.3.3 Active Galactic Nuclei

As the bright centers observed in some galaxies, these compact cores are emitters of extreme energies, making them prime candidates for UHECR acceleration. It is accepted that AGN are driven by SMBH central engines. These black holes are described by the Kerr metric, giving them a spin and a corresponding angular momentum [34]. Through interactions of infalling material and magnetic fields, the rotational energy can be extracted to form highly relativistic jets [35]. In the plane of rotation surrounding the central mass, one usually finds an accretion disk emitting luminous thermal radiation, a thorough review of which is given by [36]. The central SMBH is enveloped by a hot plasma of low density, defining the so-called corona region.

Included in [37] is a brief overview of the unified AGN model that assumes a generally similar structure for all active galactic cores. In this view, distinct AGN types are differentiated by their radio emissivity and total luminosity, as well as the relative orientation in the direction of an observer. The last feature predicts the measured effects of broad and narrow line regions or the obstruction by a dusty torus that is situated around the outer accretion disk. Potential sources of high-energy neutrinos in the complex AGN environment are discussed in [38]. This thesis assumes a general DSA mechanism, which injects energetic particles onto a static accretion disk as the proton target. The shocks involved in this acceleration have several possible origins, such as the corona or the disk itself. Other options are jet shocks that travel towards the inner region or starburst events in the surrounding galaxy as tested in [39]. One more critical assumption is that of vanishing magnetic fields inside the AGN disk, which is necessary to neglect synchrotron losses. At first order, this is justified by the same reasoning given for the magnetar setting.

2.3.4 Accretion Disks

Diffusely distributed material in orbit around a central massive object naturally produces flat structures. This is a consequence of gravitational forces being compensated in the radial plane by rotational effects while matter is relatively free to collapse in the axial direction. Compression and friction during inward spiraling heat the disk, thereby emitting intense thermal radiation. Settings where these phenomena likely occur are the protoplanetary disks that surround newly formed stars or accretion flows on a SMBH at the center of a galactic core region, among others. The following describes some related effects that are also discussed in [21].

In Newtonian physics, the gravitational force at distance R from a mass M is given as

$$F = \frac{GMm}{R^2} \quad (11)$$

for particles with masses m orbiting the central object. The resulting acceleration is therefore of magnitude $g = GM/R^2$ with vertical component $\ddot{z} = g \sin(\vartheta)$ and ϑ as the angular elevation. In case of $\vartheta \ll \pi/2$ one can approximate $\sin(\vartheta) = z/R$ to obtain

$$\ddot{z} = \frac{GMz}{R^3}$$

which is related to pressure p and density ρ via $dp/dz = -\rho\ddot{z}$ for a stable hydrostatic equilibrium to exist. Using the speed of sound $u^2 = dp/d\rho$ allows reformulation to

$$\frac{d\rho}{dz} = -\rho \frac{GMz}{u^2 R^3} \quad (12)$$

and $\rho = \rho_0 \exp(-z^2/2h^2)$ after integration. According to this result, the height h defined via

$$h^2 = \frac{u^2 R^3}{GM} \quad (13)$$

gives the standard deviation of the density, which follows a centered Gaussian distribution.

Assuming $M \gg m$ and circular Keplerian orbits, expression (11) equals the acting centripetal force, leading to $v^2 = GM/R$ for the orbital velocity. From writing $h^2 = u^2 R^2 / v^2$ and the small angle approximation $h \ll R$ follows $u \ll v$ as a necessary condition, meaning that the orbital velocity must greatly exceed the speed of sound specific to the medium. This special case is called a thin disk and can further be extended to slim or even thick types of accretion structures.

Any luminous object radiating with spherical symmetry exerts a pressure

$$P = \frac{L}{4\pi R^2 c}$$

as a function of luminosity L at distance R from the source. Suppose a gaseous cloud containing particles with masses m is falling towards the same bright central mass M due to gravitational attraction. During this process, each particle experiences $F = \kappa m P$ as an opposing radiative force, where the opacity κ represents cross section per unit mass. Balancing (11) leads to

$$L = \frac{4\pi G M c}{\kappa}$$

as the Eddington luminosity limit, beyond which additional matter is immediately blown away from the central object. By assuming that the infalling material consists exclusively of ionized hydrogen, one can approximate $\kappa = m/\sigma$ with the Thomson cross section σ from scattering of electrons and m as the proton mass. Though originally applied in the context of stellar structures, this approach can also be used to describe accretion disks. If a compact object increases its mass with rate \dot{M} due to accreting matter, some of the corresponding gravitational potential may be converted to radiation. In terms of rest energy, a luminosity of $L = \eta \dot{M} c^2$ is obtained where a factor η denotes the efficiency of this mechanism. With (2.3.4) one finds

$$\dot{M} = \frac{4\pi G M}{\eta c \kappa}$$

as an analogous steady state limit for the accretion rate, enforced by continuous balancing of radiation pressure and gravitational forces as an intrinsic feedback process.

3 Methods

Building on a physical background, this chapter first introduces generally applicable methods for the translation of an injected proton distribution to a hadronic spectrum, which then decays to create neutrinos. Subsequently, the injection spectra are described for the previously specified astrophysical settings. To start with, a general case $a \rightarrow b$ is defined for the reaction. Given a spectrum dN_a/dE_a that describes the number N_a of particles a per E_a energy interval, as well as the spectral distribution $F_{a \rightarrow b}$ for the probability that particles b are produced by a singular interaction, one can solve the folding integral

$$\frac{dN_b}{dE_b}(E_b) = \int_{\hat{E}_a}^{\hat{E}_a} dE_a \frac{dN_a}{dE_a}(E_a) F_{a \rightarrow b}(E_b, E_a) \quad (14)$$

to obtain their numbers N_b with respect to E_b energies. From this formulation, it is clear that both distributions and spectra should be assumed to depend on energy, with other arguments such as the time t being allowed as well. Additionally, integration bounds $\check{E}_a \leq \hat{E}_a$ must always be specified, which are usually dictated by kinematic constraints.

To implement and compute all following parametrizations, the *Python* programming language and its library *NumPy* are used. Graphical results are created via the *Matplotlib* package.

3.1 Cross Sections

By defining an effective area perpendicular to the momentum vectors of projectiles and targets, cross sections as described in Section 2.1.4 measure probabilities of collision processes in particle physics and are therefore required for the calculation of spectral distributions. Distinctions of particle and antiparticle cross sections vanish at high energies and are therefore omitted [19].

3.1.1 Scattering

To model total cross sections in hadron-proton scattering, this thesis uses the formula

$$\sigma_{hp} = H_h \ln^2(s/s_h) + P_h + R_h^1(s_h/s)^{\eta_1} + R_h^2(s_h/s)^{\eta_2} \quad (15)$$

as given in [40] for a universal analytic parametrization of the corresponding amplitudes. All adjustable parameters are listed in table 1 together with relevant meson lifetimes for cooling. In this approach, the variable M relates to $H = \pi(\hbar c/M)^2$ and $s_h = (m_h + m_p + M)^2$ as an effective mass. Coefficients in (15) are named after Heisenberg, Pomeranchuk and Regge, respectively, and have some qualitative motivation, though the formula itself is mainly a quantitative result.

TABLE 1: Fits to the total inclusive scattering cross sections in hadron-proton collisions. Parameters are taken from [40] with $M = 2.121$ GeV for $H = 0.272$ mb as the rate of growth. Both $\eta_1 = 0.447$ and $\eta_2 = 0.5486$ are dimensionless exponents. Decay times τ_h and rest masses m_h can be found in the particle listings [19] where the latter are given in natural units.

h	P_h / mb	R_h^1 / mb	R_h^2 / mb	τ_h / ns	m_h / GeV	s_h / GeV^2
p	34.41	13.07	7.39		0.938	15.98
π	18.75	9.56	1.767	26.03	0.140	10.23
K	16.36	4.29	3.408	12.38	0.494	12.62

Assuming a quasi universal ratio \mathcal{R} between elastic and total hadron cross sections, one obtains the inelastic cross section $\sigma_{\text{inel}} = (1 - \mathcal{R})\sigma_{\text{tot}}$ from $\sigma_{\text{el}} = \mathcal{R}\sigma_{\text{tot}}$ and $\sigma_{\text{el}} + \sigma_{\text{inel}} = \sigma_{\text{tot}}$ as a unitarity condition. Provided in [41] is the model-independent parametrization

$$\mathcal{R}(s) = \frac{\sigma_{\text{el}}(s)}{\sigma_{\text{tot}}(s)} = \mathcal{A} \tanh(\gamma_1 - \gamma_2 \ln(s) + \gamma_3 \ln^2(s)) \quad (16)$$

with a constant asymptote \mathcal{A} at very high energies. Coefficients are given in Table 2 for different physical settings. Both equations (15) and (16) use units of GeV^2 for the s variables. Combining these, Figure 1 depicts the scaling of inelastic cross sections with energy for different hadrons.

TABLE 2: Almost model-independent ratio of hadronic elastic and total scattering cross sections. Factors γ are taken from [41] for varying \mathcal{A} asymptotes.

\mathcal{A}	γ_1	γ_2	γ_3
1/2	0.466	0.0259	0.00177
1	0.2204	0.0111	0.00076

Reference [42] examines the asymptotic rise $\sigma(s) \propto \ln^2(s)$ derived in [43] as a theoretical upper bound and concludes that it is somewhat exceeded. Additionally, an asymptote $\mathcal{A} = 1/3$ due to diffraction as opposed to the black disk limit $\mathcal{A} = 1/2$ from optical theorem predictions is suggested in [42]. As parameters are only available in the latter case, all calculations of \mathcal{R} use a ratio (16) as defined by $\mathcal{A} = 1/2$ for this thesis. Data matching $\mathcal{A} = 1/3$ imply that $\sigma_{\text{inel}}(s)$ is slightly underestimated, though this is unlikely to noticeably impact the overall results.

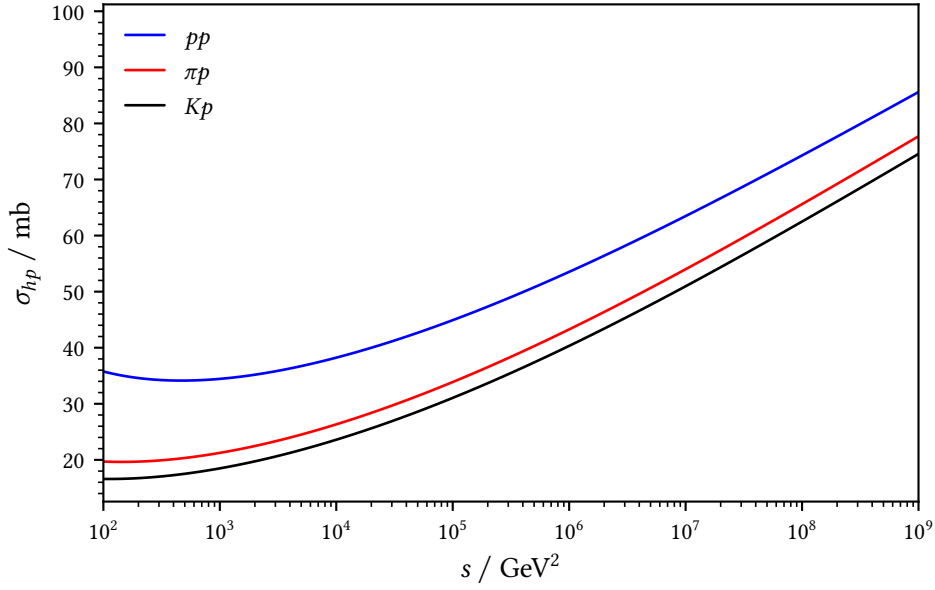


FIGURE 1: Inelastic cross sections σ_{hp} for hadron-proton scattering according to the parametrizations (15) and (16) reproducing an asymptotic $\ln^2(s)$ scaling.

3.1.2 Production

For charm quark production in proton-air collisions, reference [44] gives

$$x_F \frac{d\sigma}{dx_F}(x_F, E_p) = ax_F^b (1 - x_F^m)^n \quad (17)$$

as the parametrized differential cross section with components

$$a = a_1 \ln(E_p) - a_2, \quad b = b_1 - b_2 \ln(E_p), \quad n = n_1 - n_2 \ln(E_p)$$

for which Table 3 lists all necessary constants. Here, proton energies E_p are defined as viewed by air nuclei at rest, while the Feynman scaling variable $x_F = p_c/p_s$ specifies the magnitude ratio of produced charm quark longitudinal momentum to all available momentum in center mass coordinates of the colliding particles. Application of Section 2.1.3 shows that this approximately fulfills $x_F = x_c$ where $x_c = E_c/E_p$ in the relevant energy ranges. It should be noted that for the values Table 3 provides, the factor $n_0 = 0.075$ from Table 1 in [44] for the lower energy regime is set to $n_0 = 7.5$ instead, because the parametrization breaks down otherwise. Further testing reveals another problem with the 10^4 GeV to 10^8 GeV region in that energies of 26 TeV or lower yield negative differential cross sections. Considering other approximations made in this thesis, it is therefore decided that an extrapolation from the 10^8 GeV to 10^{11} GeV case to all energies can be done without producing unreasonably large errors. With these parameters, equation (17) only becomes negative for energies of 140 GeV and below.

TABLE 3: Parametrization of the weighted charm quark production differential cross section. Coefficients are calculated from [44] to write E_p in units of GeV without needing redundant conversion steps. The exponent $m = 1.2$ is a constant at all energies. For the application at hand, energy ranges beyond the given validity intervals are used as mentioned in the text.

E_p / GeV	$a_1 / \mu\text{b}$	$a_2 / \mu\text{b}$	b_1	b_2	n_1	n_2
$10^4 - 10^8$	826	8411	0.197	0.016	8.486	0.107
$10^8 - 10^{11}$	403	2002	0.237	0.023	7.639	0.102

Adopting linear scaling with respect to the nucleon number from [45] gives

$$\frac{d\sigma}{dx_c}(x_c, E_p) = \tilde{A}^{-1} \frac{d\sigma}{dx_F}(x_c, E_p)$$

for inclusive charm production in proton-proton collisions. Approximating air as a gas mixture of roughly 75% nitrogen and 25% oxygen, one finds $A = 14.5$ for this factor. By integrating the charmed hadron cross section defined below and comparing to experimental data in [46] for the charm mesons considered in this thesis, one finds that calculated values exceed measurements by a factor 22.32 ± 2.34 on average, yielding $\tilde{A} = 323.64$ as a modification to enforce compatibility with observations. One problem of this approach is that [46] provides values at $\sqrt{s} = 13$ TeV or roughly $E_p = 90$ PeV only, so that deviations at different energies are not accounted for. Similar to earlier reasoning, the resulting inaccuracy is deemed acceptable.

Translation of charm quarks to charmed hadrons is achieved with an integral

$$\frac{d\tilde{\sigma}}{dx_h}(x_h, E_p) = \int_{x_h}^1 dz z^{-1} \frac{d\sigma}{dx_c}(x_c, E_p) D_c^h(z) \quad (18)$$

where $z = E_h/E_c$ and $x_h = E_h/E_p$ as well as $x_c = x_h/z$ are fractional energies. Limits for the integration follow from a basic inequality $E_h \leq E_c \leq E_p$ to incorporate kinematic constraints. Furthermore, the probability of observing any final state h originating from a c quark is encoded in a *Fragmentation Function* (FF) $D_c^h(z)$ dependent on the fraction of hadron to charm energy. Reference [47] addresses the connection between this concept and that of a *Parton Distribution Function* (PDF) among other things. While a PDF represents the probability density of finding a parton with given momentum inside a colorless particle, probabilities for color-neutral states existing in individual partons are given by the appropriate FF instead. The partons described here are either quarks or gluons, which Sections 2.1.1 and 2.1.2 characterize in more detail.

By fitting to existing data or perturbative calculations, models can extrapolate to low momentum fractions that have not yet been probed experimentally. Such a method has lead [48] to obtain

$$D_c^h(z) = \frac{N_h z(1-z)^2}{((1-z)^2 + \epsilon_h z)^2} \quad (19)$$

with parameters from e^+e^- data in table 4 as the charm hadron FF used throughout this thesis. It is important to note that such functions are invariant under charge conjugation, so that there is no differentiation between quark to particle or antiquark to antiparticle processes.

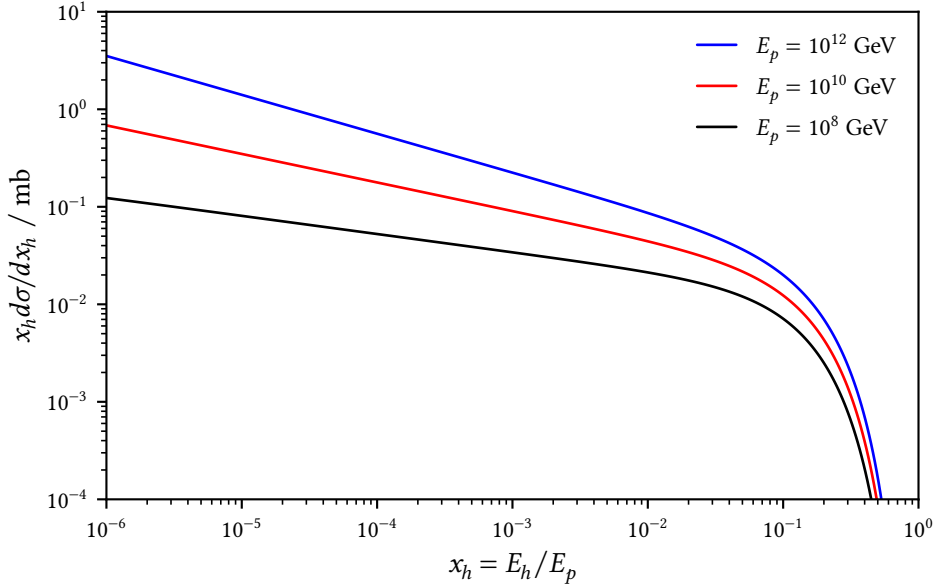


FIGURE 2: Weighted energy differential cross sections for $pp \rightarrow D^0 X$ production at different proton energies E_p according to the (20) parametrization.

To account for kinematic constraints, one final modifier has to be included at this point. Because collisions must provide enough energy for particle formation, charmed hadron energies cannot be lower than their rest masses, leading to $E_h \geq m_h$ as a natural condition. With Table 4 listing these mass parameters, a cutoff similar to that in [49] is introduced, rewriting (18) to

$$\frac{d\sigma}{dx_h}(x_h, E_p) = \frac{d\tilde{\sigma}}{dx_h}(x_h, E_p) \left(1 - \frac{m_h}{x_h E_p}\right)^{1/2} \quad (20)$$

where $E_h = x_h E_p$ ensures physical kinematics are respected. It turns out that this expression is integrable, whereas the unmodified version (20) is not. Figure 2 depicts the D^0 differential cross section for different incident proton energies and fixed protons as targets. Comparing this to Figure 7 in [14] indicates similar shapes, though our parametrizations result in less flat distributions at low x_h values.

3.2 Spectral Distributions

Constructing spectra dN_h/dE_h from proton injection requires folding of $F_{p \rightarrow h}$ as the hadronic distribution for a single pp interaction with the number of protons per energy interval given by the function dN_p/dE_p obtained from source-specific modeling. An analogous approach can be applied to compute neutrino spectra dN_ν/dE_ν from dN_h/dE_h via distributions $F_{h \rightarrow \nu}$ formulated according to the involved decay modes. Equation (14) describes exactly this, with the following section providing all required distributions.

3.2.1 Charm

Spectral distributions for charmed hadron production are calculated according to [14] through

$$F_{p \rightarrow h}(E_h, E_p) = E_p^{-1} \sigma_{pp}^{-1}(E_p) \frac{d\sigma}{dx_h}(x_h, E_p),$$

with $E_h = x_h E_p$ translating between variables. This can be understood as effectively normalizing term (20) with respect to the energies and inelastic cross sections of protons, which are scattered as described in Section 3.1.1 to yield hadron numbers per unit energy and collision.

To find neutrino spectra from charmed hadrons, the same approach as in [50] is used, which assumes an effective energy distribution approximated by three-body decays for the semileptonic channel to a less massive pseudoscalar meson. By neglecting lepton masses, one obtains

$$\tilde{F}_{h \rightarrow \nu}(y) = D_h^{-1} \left(6b_h a_h^2 - 4a_h^3 - 12\lambda_h^2 a_h + 12\lambda_h^2 y - 6b_h y^2 + 4y^3 + 12\lambda_h^2 \ln((1-y)/\lambda_h) \right)$$

as a distribution with $y = E_\nu/E_h$ and $F_{h \rightarrow \nu}(E_\nu, E_h) = \mathcal{F}_h \tilde{F}_{h \rightarrow \nu}(y)/E_h$ for conversion.

Hadron specific coefficients for this equation are defined with the parameter $\lambda_h = \tilde{s}_h/m_h^2$ as

$$a_h = 1 - \lambda_h, \quad b_h = 1 - 2\lambda_h, \quad D_h = 1 - 8\lambda_h - 12\lambda_h^2 \ln(\lambda_h) + 8\lambda_h^3 - \lambda_h^4$$

where both s_h and m_h are listed in Table 4 for all included charmed hadrons. The assumption of three-body decays like $D^+ \rightarrow \bar{K}^0 e^+ \nu_e$ can be justified by consulting [19] for information on the relevant particles and comparing branching ratios, which indicate that purely leptonic modes are strongly suppressed. Hadronic channels such as $D^+ \rightarrow \pi^+ \pi^0$ or $D^+ \rightarrow K^- \pi^+ \pi^+$ are either very improbable as well or occur at significant rates but do not contribute many high-energy neutrinos due to pions and kaons being subject to further cooling before decaying to leptons. By a similar logic, secondary muon decay is neglected when determining the neutrino spectrum, as muons would experience additional cooling before decaying and because charm cross sections are already low compared to other mesons.

TABLE 4: Coefficients for charm hadron production, cooling and decay to neutrinos.

All parameters ϵ_h are taken from leading order QCD fits via the FF as defined and described in [48] with normalizations N_h given by [14] to rescale the integration of (19) over $[0,1]$ to approximately match the fractions f_h provided in [51] from measurements. Effective masses $\sqrt{s_h}$ and branching fractions F_h are determined by [52] and [50] from fitting decay rates. Mean lifetimes τ_h and masses m_h are adopted from [19] in the particle listings. Mass type quantities use natural units.

h	N_h	ϵ_h	τ_h / fs	F_h	$\sqrt{s_h}$ / GeV	m_h / GeV
D^0	0.577	0.101	410	0.067	0.67	1.86
D^+	0.238	0.104	1033	0.176	0.63	1.87
D_s^+	0.0327	0.0322	501	0.065	0.84	1.97
Λ_c^+	0.0067	0.00418	203	0.045	1.27	2.29

3.2.2 Pions & Kaons

By parametrizing SIBYLL [53] results, a neutral pion production spectrum of the form

$$\tilde{F}_{p \rightarrow \pi}(x_\pi, E_p) = 4\alpha B x_\pi^{\alpha-1} \left(\frac{1 - x_\pi^\alpha}{1 + r x_\pi^\alpha (1 - x_\pi^\alpha)} \right)^4 \left((1 - x_\pi^\alpha)^{-1} + \frac{r(1 - 2x_\pi^\alpha)}{1 + r x_\pi^\alpha (1 - x_\pi^\alpha)} \right) \left(1 - \frac{m_\pi}{x_\pi E_p} \right)^{1/2}$$

is found in [49] with $m_\pi = 0.135$ GeV [19] translated to natural units and parameters

$$B = \tilde{B} + C, \quad \alpha = \frac{\tilde{\alpha}}{\sqrt{C}}, \quad r = \frac{\tilde{r}}{\sqrt{C}}$$

where a low energy cutoff is enforced via $E_\pi = x_\pi E_p$ in the mass term. From

$$C = c_1 - c_2 \ln(E_p) + c_3 \ln^2(E_p)$$

results a dependence on projectile energy for the shape of this distribution.

Coefficients are specified in Table 5 and recalculated from E_p in TeV to units of GeV instead. Under the assumption of a π^0 cross section approximately equal to the π^\pm average and with identical spectra between charged pions, it follows that $F_{p \rightarrow \pi} = \tilde{F}_{p \rightarrow \pi}/E_p$ should describe pion production regardless of charge reasonably well for the purpose of this thesis.

TABLE 5: Parametrized spectral distribution for neutral pion production. Factors are taken from [49] and converted to write E_p in GeV for the unitless c_k coefficients.

\tilde{B}	$\tilde{\alpha}$	\tilde{r}	c_1	c_2	c_3
0.25	0.98	2.6	1.515	0.206	0.075

For a convenient formulation of kaon production, references [54] and [55] indicate a constant ratio π/K at moderately high energies. Similar fractions are retrieved from multiplicities given in [56] and lead to $F_K/F_\pi = 0.12$ as a simplifying assumption, the validity of which cannot be guaranteed for the application at hand. Calculations of kaon spectra still employ this approach but are subject to considerable reservations as a result, because fixed ratios to pion spectra are unlikely to be universal. Other than this factor, the pion mass is replaced with that of kaons for a correct cutoff in the above expression.

Decays of pions and kaons to neutrinos are approximated via the $h \rightarrow \mu^+ \nu_\mu$ two-body channel with branching fractions of $\mathcal{F}_\pi = 99.99\%$ and $\mathcal{F}_K = 63.56\%$ given in the [19] particle listings. By decaying, muons produced in these processes can significantly impact the neutrino spectrum. Results from [14] suggest that this is particularly relevant for pions. Muonic three-body decays of type $\mu^- \rightarrow e^- \bar{\nu}_e \nu_\mu$ as well as cooling factors depend on the polarization of participating leptons due to the nature of weak force coupling. This complicates computations and is thus omitted for the purpose of restricting the present thesis to a manageable scope, though it should be remembered as an important caveat for the final results.

The remaining two body-decays of ultra-relativistic hadrons h to leptons l obey a distribution

$$F_{h \rightarrow l}(E_l, E_h) = \mathcal{F}_h E_h^{-1} (1 - \lambda_h)^{-1}$$

with $m_\nu = 0$ and $m_\mu = 0.106$ GeV [19] as well as $\lambda_h = m_\mu^2/m_h^2$ as a parameter. This formula is the same whether $l = \nu$ or $l = \mu$ because there is one muon for each neutrino. In addition, kinematic considerations lead to $E_\mu/E_h > \lambda_h$ and $E_\nu/E_h < 1 - \lambda_h$ for bounds $E_\mu < E_h < E_\mu/\lambda_h$ in case of muons or corresponding limits $E_\nu/(1 - \lambda_h) < E_h < E_p$ when considering neutrinos, which are required by (14) for integration.

3.3 Computation

Taking into account previous deliberations, this section now combines these with the contents of Chapter 2 to give explicit steps for calculating the desired results, as well as numerical values for the required parameters. Additionally, some notes on the implementation are included.

3.3.1 Injection

The proton spectrum model of young magnetars described in Section 2.3.1 starts with an idealized charge density $\rho = \omega B_{\text{ns}}/(2\pi c)$ derived from [31] and leads to $n = \rho/e$ for the number of charge carriers. Integrating over the so-called polar caps defined by a radius $R_{\text{pc}} = R_{\text{ns}} \sqrt{R_{\text{ns}}/R_{\text{lc}}}$ from which open field lines originate and taking a monochromatic energy according to (10) for all times t results in a time-derivative delta-functional spectrum

$$\frac{d\dot{N}_p}{dE_p}(t, E_p) = \frac{B_{\text{ns}} R_{\text{ns}}^3 \omega_0^2}{ec(1 + t/t_{\text{sd}})} \delta(E_p - E^M(t)) \quad (21)$$

that is compatible with a $dN_p/dE_p \propto E_p^{-1}$ power law.

For the AGN setting, a more general DSA scenario like in Section 2.2.3 is assumed, yielding

$$\frac{dN_p}{dE_p}(E_p) = SE_p^{-2}$$

with S for an arbitrary normalization factor that does not need to be specified further, as this thesis is interested in relative neutrino contributions instead of absolute predictions.

3.3.2 Production & Decay

Spectra of hadrons and neutrinos are generally computed as in (14) via folding, though for the hadronic spectrum, a cooling factor (1) and optical depth (2) are included, giving

$$\frac{dN_h}{dE_h}(E_h) = C\mathcal{O} \int_{E_h}^{\mathcal{E}_p} dE_p \frac{dN_p}{dE_p}(E_p) F_{p \rightarrow h}(E_h, E_p)$$

with maximum proton energies \mathcal{E}_p as a result. Because the proton spectrum (21) contains a delta function $\delta(E_p - E^M)$ in the magnetar case, integration over E_p simply substitutes E^M in place of the proton energy. Accordingly, a limit $\mathcal{E}_p = \infty$ can be set to ensure $E^M < \mathcal{E}_p$ at all times. For the AGN accretion disk, a choice of $\mathcal{E}_p = 10^{12}$ GeV is made in accordance with the maximum magnetar proton energy. A value exceeding that of the GZK cutoff at $E_p = 10^{11}$ GeV described in Section 2.2.2 can be justified by assuming close proximity to the origin of accelerated particles. Proceeding from this, cross sections and distributions are taken from Sections 3.1 and 3.2 to translate the produced hadron population to neutrinos, which due to their weak interactions mentioned in Section 2.1.2 are assumed to be unaffected by attenuation.

Cooling factors (1) vary for different hadrons, as $t_{\text{dec}} = \tau_h E_h / m_h$ and $t_{\text{cool}} = (\kappa_{hp} \sigma_{hp} n c)^{-1}$ define the decay and cooling timescales, with parameters τ_h and m_h listed in the respective tables, as well as (15) and (16) giving the σ_{hp} cross sections, which are approximated to those of kaons for charmed hadrons. The effective optical depth (2) only describes proton interactions, with a mean free path $\lambda_{pp} = (\kappa_{pp} \sigma_{pp} n)^{-1}$ and distance d determined by the specific model. Inelasticity factors $\kappa_{hp} = 0.8$ and $\kappa_{pp} = 0.5$ are assumed to be constants as given in [14]. For the scenario of a newborn magnetar, properties of the ejecta determine $n = n_{\text{ej}}$ (3) and $d = r_{\text{ej}}$ (4) as parameters. The AGN accretion disk is modeled by the height parameter (13) that varies with radius and characterizes a diffuse density distribution, as well as the angle α measuring the direction of incidence relative to the disk plane. This is further simplified by assuming a sharply bound region of height h with homogenous density, leading to $d = h / \sin \alpha$ as the distance travelled by a particle. Because results are insensitive to variations in distance, one can set $\alpha = \pi/2$ to find $\sin \alpha = 1$ and $d = h$ with $h = 10^{15}$ cm taken from [57]. Typical number densities of the order 10^{15} cm^{-3} in the disk plane [58, 59] are scaled down to account for the inhomogenous distribution (12) and taken to be $n = 10^{14} \text{ cm}^{-3}$ for the following calculations. To put this into perspective, typical SMBH masses of around $10^8 M_\odot$ lead to a 10^{13} cm Schwarzschild radius. While accretion disks might extend up to 10^{18} cm radii, jets can reach multiple 100 kpc with terminal bow shocks at Mpc distances from the core [35, 38, 57].

Parameters for the magnetar setting are adopted from [14]. Neutron star radii $R_{\text{ns}} = 10^6$ cm and masses $M_{\text{ns}} = 1.4 M_{\odot}$ in accordance with the Chandrasekhar limit that defines the maximum stable mass for white dwarfs lead to $I_{\text{ns}} = 10^{45}$ g cm² as the classical moment of inertia for a rigid homogenous sphere, where relativistic effects are ignored and $1 M_{\odot} = 2 \times 10^{33}$ g is used. Reference [60] provides the minimum period of uniform rotation, beyond which the neutron star loses its structural integrity. Choosing twice this value yields $\omega_0 = 10^4$ s⁻¹ as an optimistic initial angular frequency. The tilt parameter χ is set to an angle of $\chi = 0.95$ radians. A magnetic field of $B_{\text{ns}} = 3.2 \times 10^{14}$ G leads to a maximum energy $E^M = 5.3 \times 10^{11}$ GeV for proton acceleration as well as $t_{\text{sd}} = 3.2 \times 10^3$ s as the spindown time. With the total ejected mass being similar to that of the respective progenitor star, values between $10 M_{\odot}$ and $35 M_{\odot}$ are possible, from which the lower bound $M_{\text{ej}} = 10 M_{\odot}$ is chosen for this scenario. At velocity $\beta_{\text{ej}} = 0.1$ of the shell, number densities $n_{\text{ej}} = 3.1 \times 10^{18}$ cm⁻³ are observed after t_{sd} has passed. Lastly, an efficiency $\eta = 0.1$ is assumed for the acceleration of protons.

3.3.3 Implementation

In order to calculate neutrino spectra from hadronic distributions, several integrals have to be computed. Discretizing this task allows the general case

$$F(x, y) = \int_{z_-}^{z_+} dz G(x, z) H(z, y)$$

to be rewritten as a Riemann sum. Assuming G and H are integrable over a given interval,

$$F_{ij} = \sum_k D_{kk} G_{ik} H_{kj}$$

converges to the exact solution for sufficiently small steps. Transforming variables

$$x \rightarrow x_i, \quad y \rightarrow y_j, \quad z \rightarrow z_k$$

and defining $D_{kk} = z_{k+1} - z_k$ leads to the above notation. It is easily shown how this expression in terms of indices translates to the product of corresponding matrices

$$\mathbf{F} = \mathbf{G} \mathbf{D} \mathbf{H}$$

as an equivalent formulation. Here, the output $\mathbf{F} \in \mathbb{R}^{m \times n}$ is obtained from the inputs $\mathbf{G} \in \mathbb{R}^{m \times l}$ as well as $\mathbf{H} \in \mathbb{R}^{l \times n}$ with the square matrix $\mathbf{D} \in \mathbb{R}^{l \times l}$ that encodes all step sizes on its diagonal. These results enable a quick and efficient implementation of the required calculations as program code, where arithmetic array operations can greatly increase execution speed. Furthermore, logarithmic spacing of \mathbf{D} often leads to better accuracy after fewer iterations. To avoid redundant computations, results are stored as data tables.¹

¹ For the purpose of reproducibility, all implementations are collected in a dedicated *GitHub* repository: github.com/fritzali/bachelor

3.3.4 Event Generators

The description of multiple colliding particle systems constitutes an extremely complex problem, which methods like perturbative QFT or lattice QCD mentioned in Sections 2.1.1 and 2.1.2 are unable to resolve with satisfactory accuracy. Modeling of collider or air shower experiments therefore requires a different approach, realized by so-called event generators that fit data in well-tested regions and extrapolate to higher energies via random sampling. The Monte Carlo event generator SYBILL used as well by [14] and [49] is optimized for the simulation of high energy cosmic ray cascades, making it a suitable choice for the calculation of cross sections in an astrophysical context such as that of this thesis [53].

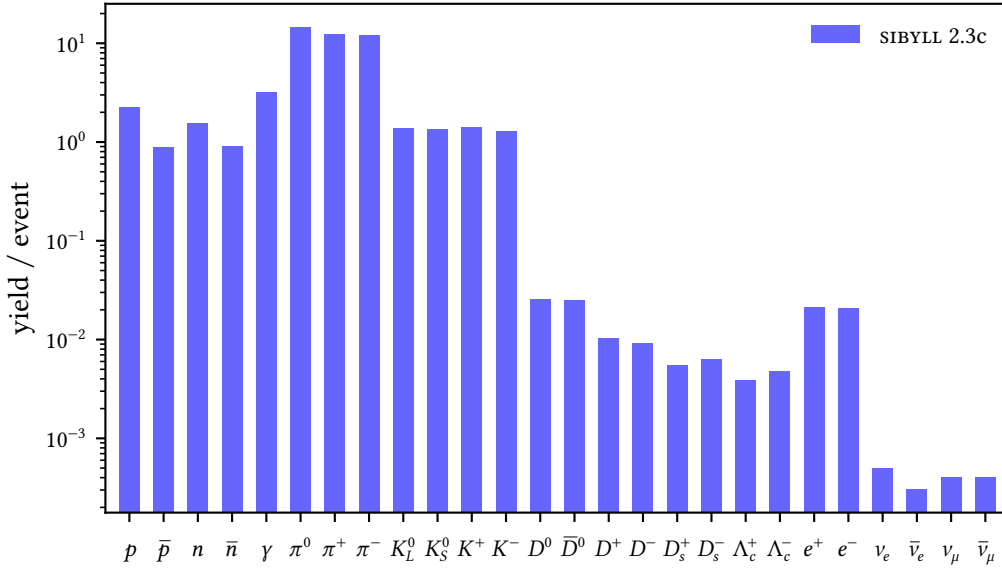


FIGURE 3: Filtered SYBILL 2.3c yields from proton-proton collisions at $\sqrt{s} = 1$ TeV center of mass energies. *Data courtesy of Marcel Schroller.*

Depicted in Figure 3 are the yields of select particle types per proton-proton collision as predicted by SYBILL 2.3c at $\sqrt{s} = 1$ TeV energies. Other particles are produced, but deemed irrelevant for modeling charm as well as pion and kaon production. This represents one step in the process of generating numerical values for the appropriate cross sections. Events are generated at discrete fixed target or center of mass energies, with individual yield populations additionally following a separate energy distribution. Accordingly, each bar in Figure 3 is an effective integral over all energies of the produced particles. Weighted energy differential cross sections $d\sigma/dx$ for specific secondary types can therefore be expressed by a histogram in two dimensions, with initial proton energies on one axis and energy of secondaries on the other. Normalizations are found by counting the yield and comparing to known values. Creating bins at the required resolutions and with sufficient statistics is computationally intensive and consumes more time than is available for work on this thesis, which instead uses parametrizations as described in the previous sections. Event generator predictions should nevertheless be considered to verify and improve upon the following results.

4 Results

Presented in this chapter are the results obtained by applying the previously described methods. Due to uncertain normalization factors, all values are given with respect to the maximum charm component in terms of flux $\dot{\phi}_\nu$, or fluence ϕ_ν , as physical quantities. By its definition,

$$\dot{\phi}_\nu = \frac{d\dot{N}_\nu/dE_\nu}{4\pi d^2},$$

the flux counts neutrinos per energy, time and area. This equation derives from evenly spreading all spectral intensity over a spherical surface with radius equal to the distance d from a single source. Integrating over time yields the fluence,

$$\phi_\nu = \frac{dN_\nu/dE_\nu}{4\pi d^2},$$

which measures neutrino numbers per energy and area instead. Because d is a constant, forming ratios of $\dot{\phi}_\nu$ or ϕ_ν eliminates it. Accordingly, the following results are distance independent. As mentioned earlier, neutrinos are not distinguished by their flavor, but by the particle decay from which they originate. Assuming identical particle and antiparticle population sizes and decay paths, resulting factors are absorbed in the normalization and require no further consideration. Model parameters use the numerical values that Section 3.3 provides.

Shown in Figure 4 is the temporal evolution of charmed hadron contributions to the total charm component at $E_\nu = 10^9$ GeV originating from a young magnetar. Decays of D^0 constitute most of the earlier charmed neutrinos, with D^+ adding significant amounts as well, especially at later times. Both D_s^+ and Λ_c^+ are roughly the same, each contributing around 10% to the combined flux. This is in line with cross sections calculated via (20) or measured by [46] as well as the respective branching fractions listed in Table 4 for effective three body decays to neutrinos.

Similarly, Figure 5 presents light curves for pions and kaons next to the total charm contribution, restricted to $E_\nu = 10^9$ GeV neutrinos. As in [14] from QCD calculations, a factor of $1/3 - 3$ is adopted for the charmed hadron uncertainty and marked with a shaded blue band. Decays of kaons generally contribute more than pions at this energy, with neutrinos from charm exceeding both by more than an order of magnitude until about $t = 10^5$ s after magnetar formation.

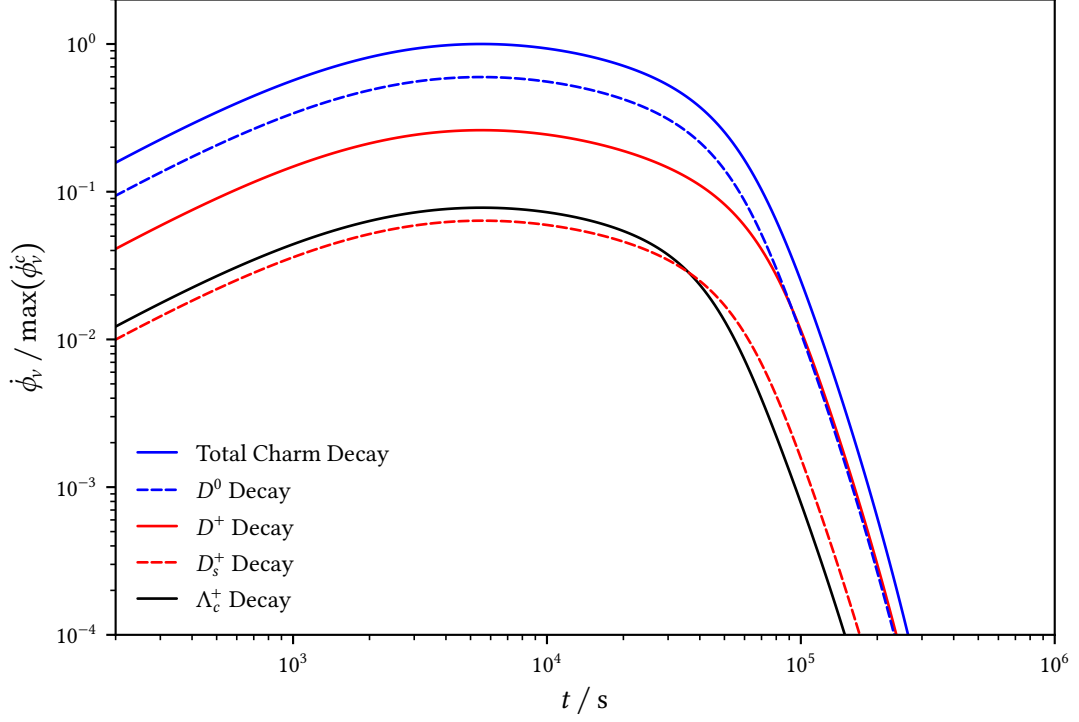


FIGURE 4: Comparison of individual charmed hadron contributions to the total charm neutrino flux at $E_\nu = 10^9$ GeV from a young magnetar, including the optical depth defined by (2) as a modification. Decays of D^0 produce most of the charmed neutrinos until later times when D^+ becomes significant, with D_s^+ and Λ_c^+ being similar, both contributing around 10% to the combined flux. This is in line with cross sections and branching fractions that Sections 3.1.2 and 3.2.1 provide.

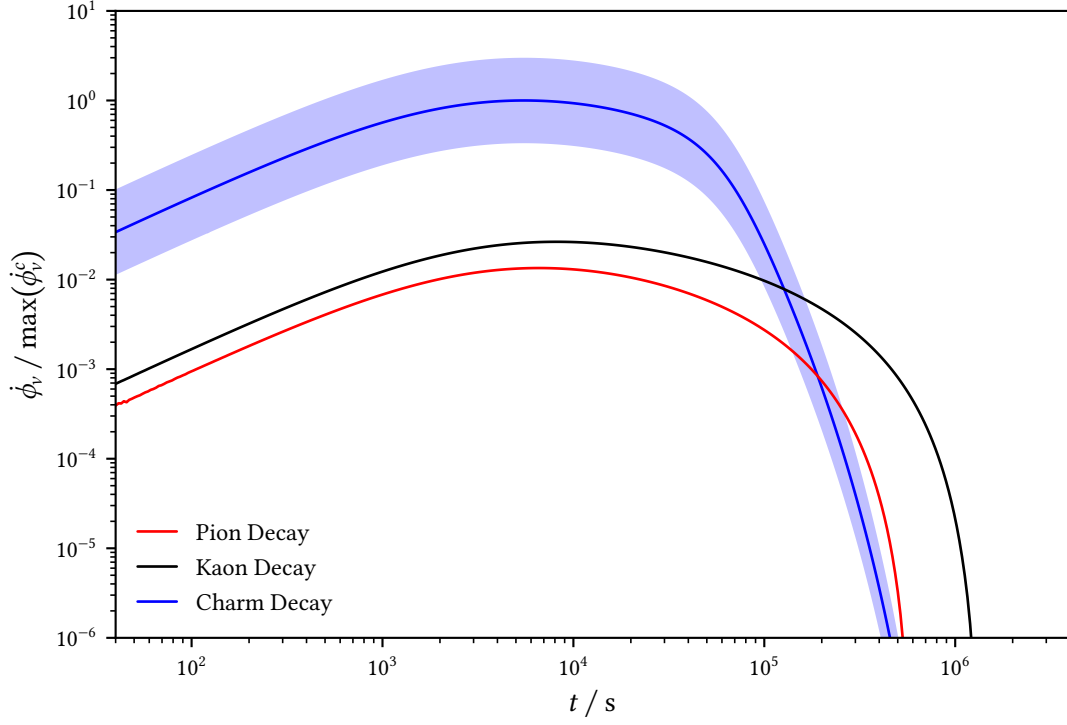


FIGURE 5: Effective neutrino light curves normalized to the maximum charm decay flux at $E_\nu = 10^9$ GeV from a newborn magnetar, including the optical depth defined by (2) as a modification. Charmed hadrons dominate up to $t = 10^5$ s with pion contributions below those from kaons at all times. A cutoff after $t = 10^6$ s occurs due to insufficient proton energies. For the charm component, a shaded error band of factor $1/3 - 3$ is adopted to replicate uncertainties from [14].

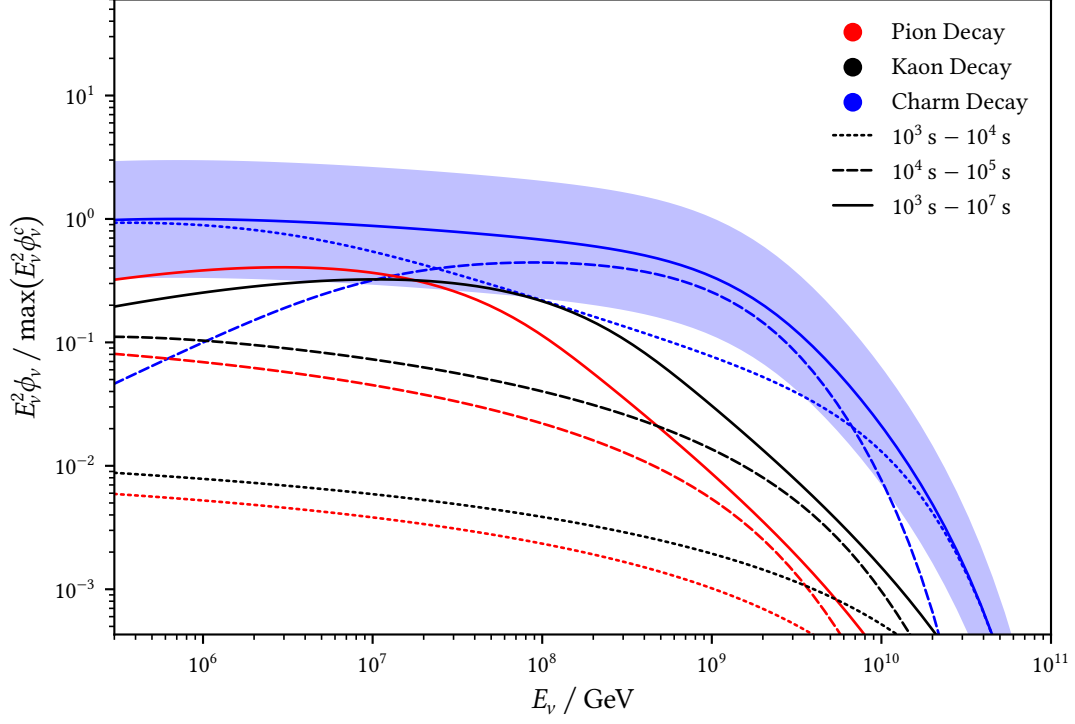


FIGURE 6: Expected neutrino fluence weighted by the charm contribution from a young magnetar for different time intervals after formation, including the optical depth defined by (2) as a modification. Charmed hadrons dominate at all energies except below $E_\nu = 10^7$ GeV for 10^4 s– 10^5 s integration. This is unexpected and therefore discussed further in the text. The same shaded uncertainty band as in Figure 5 is adopted for charm decays. Fluences are scaled by a factor E_ν^2 for clarity and to facilitate the comparison to [14].

4 Results

In order to evaluate the significance of different time periods, Figure 6 depicts integration results over varying intervals for pion, kaon and charm fluence. Contrary to expectations, charmed hadron decays are dominant at all energies by as much as one order of magnitude. Comparing Figures 5 and 6 with the corresponding plots in [14] reveals further inconsistencies. Notably, light curves in Figure 5 have relatively flat slopes at earlier times, and the charm neutrino fluence in Figure 6 shows no decrease towards lower energies. Testing different potential error sources indicates that the optical depth \mathcal{O} is most likely responsible for these discrepancies. Inserting proportionalities of ejecta density $n_{\text{ej}} \propto t^{-3}$ and radius $r_{\text{ej}} \propto t$ into (2) while assuming σ_{pp} to be constant leads to an approximate $\mathcal{O} \propto t^{-2}$ dependence and results in neutrino numbers being distorted significantly towards larger values at earlier times. To verify this finding, calculations are repeated under omission of the optical depth.

As suspected, these results more closely match those in [14]. Starting with the comparison of charmed hadrons, Figure 7 agrees with the previous statements regarding D^0 and D^+ dominating over D_s^+ and Λ_c^+ decays. By excluding the optical depth, one can reveal additional information via the identification of comparatively narrow peaks. Their relative positions are consistent with the different mean lifetimes that Table 4 lists, an observation which is not accessible from Figure 4 due to flux curves resembling broad plateaus rather than clearly defined extrema. Due to shorter decay times resulting in vanishing cooling effects (1) at higher energies, curves are shifted to reproduce slight offsets in charmed hadron contribution.

Again comparing [14] to Figures 8 and 9 indicates improved agreement, with distribution shapes that are roughly similar in both cases. Because of differences in the approaches, some deviation is to be expected. Reference [14] uses event generator results to model pion and kaon cross sections, as well as QCD calculations for the charm component, while this thesis collects various parametrizations from the literature for semianalytical computations instead. Especially the almost identical shapes of pion and kaon light curves in Figure 8 are most likely a consequence of the simplifying assumption that their spectral distributions are linearly proportional except for a cutoff determined from their rest masses. Despite this, neutrino fluxes from pion or kaon decay individually fit their counterparts in [14] fairly well when the contribution from muons is ignored, and their respective maxima are within acceptable margins compared to the charmed hadron curves in Figure 8 and reference [14].

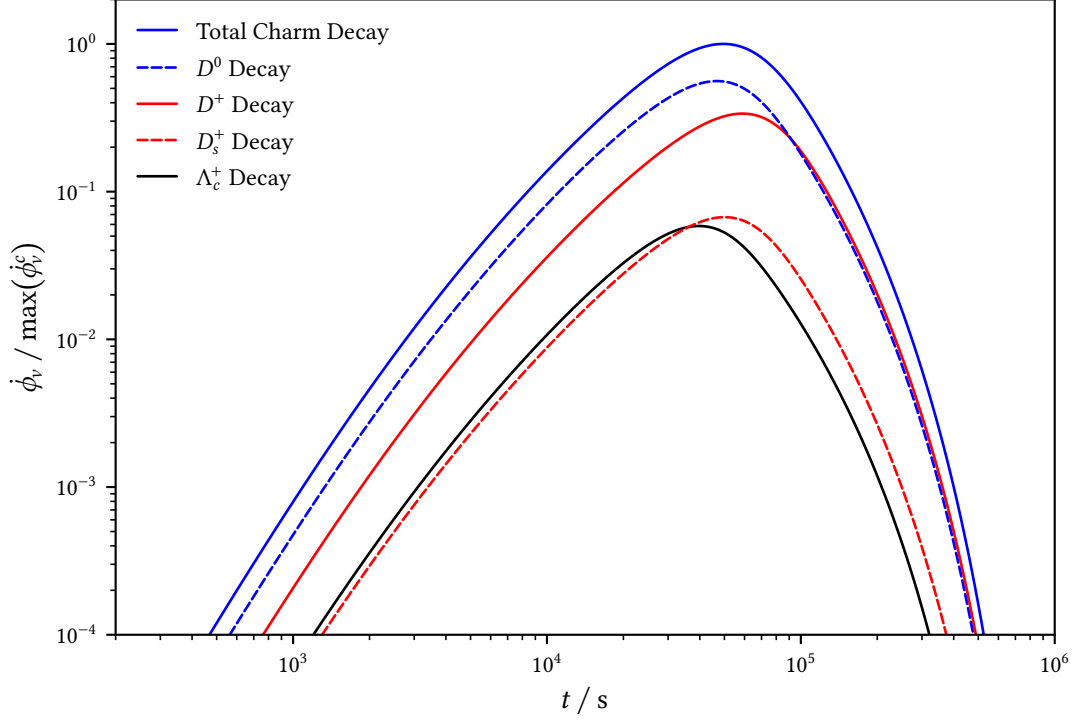


FIGURE 7: Comparison of individual charmed hadron contributions to the total charm neutrino flux at $E_\nu = 10^9$ GeV from a young magnetar, excluding the optical depth defined by (2) as a modification. Properties of hadronic components in agreement with Figure 4 are observed. Additionally, positions of maxima compatible with lifetimes given in Section 3.2.1 can be identified, as Λ_c^+ has the shortest decay timescale and therefore peaks earliest, while D^+ reaches its maximum after all other charmed hadrons due to its longer lifetime.

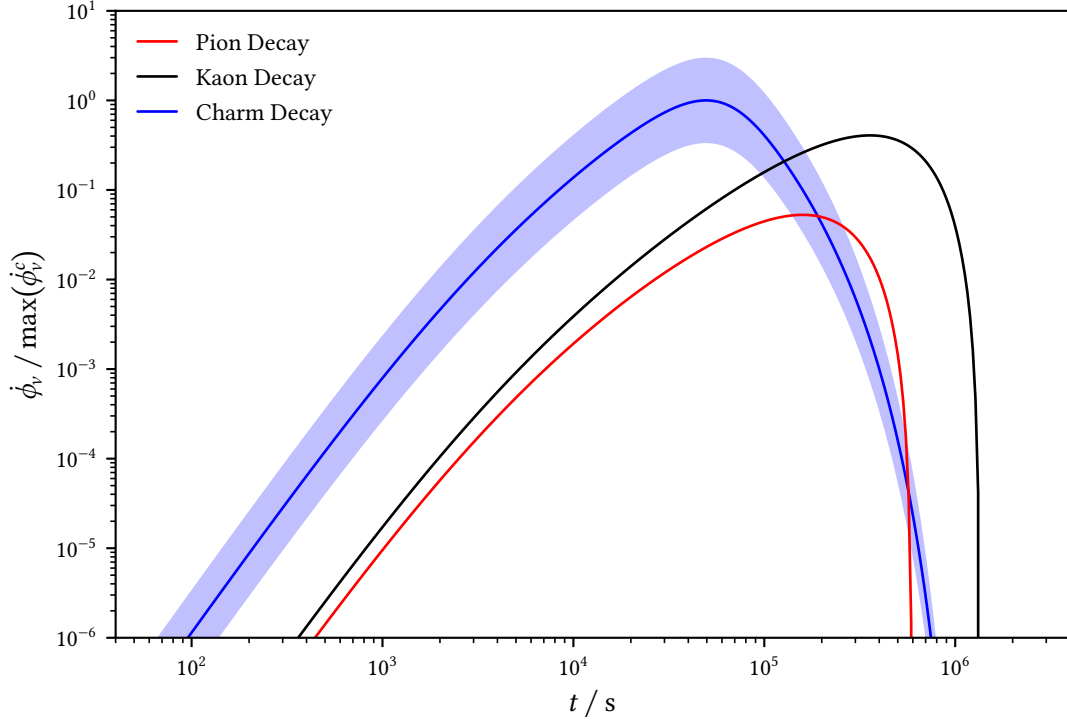


FIGURE 8: Effective neutrino light curves normalized to the maximum charm decay flux at $E_\nu = 10^9$ GeV from a newborn magnetar, excluding the optical depth defined by (2) as a modification. Properties of hadronic components in agreement with Figure 5 are observed. Different shapes that are also seen in Figure 7 agree with cooling and the omission of an optical depth as Section 2.1.5 describes, and lead to pion and charm peaks with larger magnitudes. The same shaded uncertainty band as in Figure 5 is adopted for charm decays.

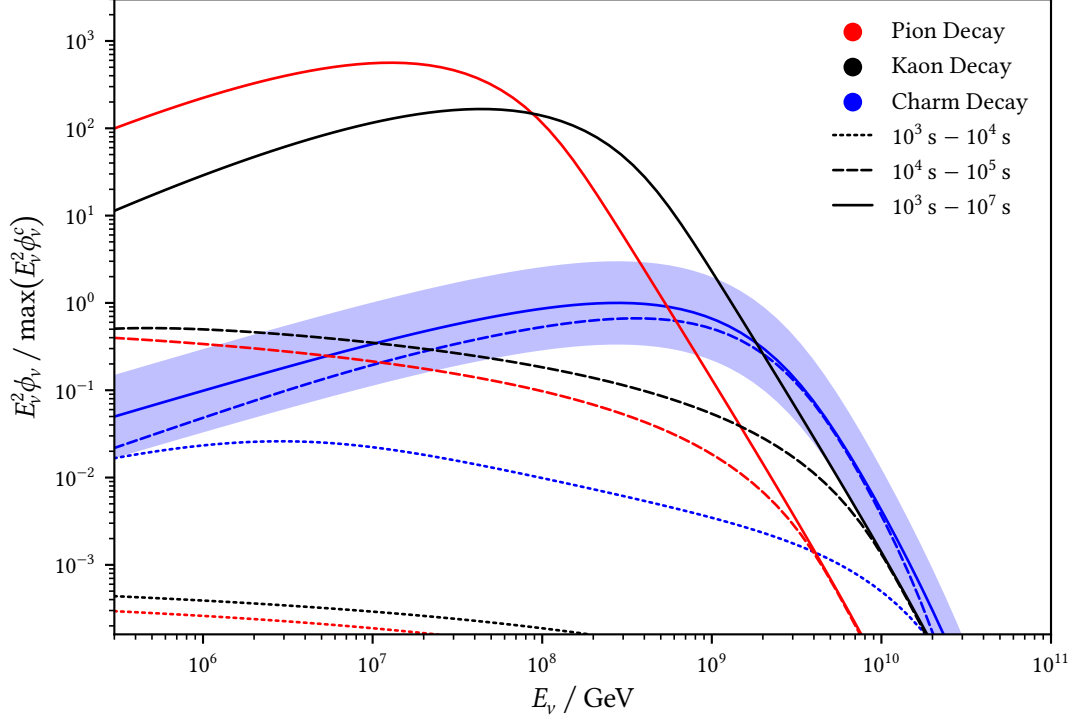


FIGURE 9: Expected neutrino fluence weighted by the charm contribution from a young magnetar for different time intervals after formation, excluding the optical depth defined by (2) as a modification. In agreement with prior expectations derived from Sections 2.3.2 and 3.2.1 for energy scaling and mean lifetimes, respectively, first pion, then kaon, and eventually charm dominate, sorted by increasing energy. The same shaded uncertainty band as in Figure 5 for charm decays as well as the scaling by E_v^2 from Figure 6 are adopted. With charmed hadrons being significant beyond $E_v = 10^9$ GeV and their lower uncertainty bound never exceeding the kaon curve, it is unclear if substantial charm signals are likely.

4 Results

There are, however, certain disagreements that are unlikely to arise purely from variations in the described methodologies. To begin with, reference [14] provides $E^M = 1.3 \times 10^{13}$ GeV as an initial value for the energy of injected protons, which disagrees with inserting the same default parameters into (10) to find $E^M = 1.7 \times 10^{12}$ GeV instead, after conversion from erg to GeV units. If the larger and seemingly erroneous value is actually used, it would imply energies an order of magnitude higher than in the calculations presented here. Predictions from this include earlier light curve cutoffs, as energies become insufficient after less time has passed, and potentially smaller separation between charm, pion and kaon components, because at each point in time, only lower energy hadrons are available for neutrino production, resulting in a reduction of otherwise possible peak values. A comparison to [14] shows that Figure 8 displays both of these features. Smaller injection energies further imply lower charm decay contributions to the total neutrino fluence, which Figure 9 seems to support as well when compared to [14]. Adding to this concern is the large divergence from Figures 5 and 6 that most likely stems from the optical depth. Setting this factor to be constant supposes a fixed fraction of protons colliding to produce hadrons, independent from density changes due to an expanding ejecta volume. Such an assumption is difficult to justify, with the potential exception of extremely high densities. As reference [14] explicitly includes an optical depth in the same way this thesis does, it is unclear how the wide disparities between neutrino spectra come about, especially considering that Figures 8 and 9 without \mathcal{O} present better matches than Figures 5 and 6 with \mathcal{O} to those in [14]. This issue represents a major incongruence and warrants further scrutiny, which the following chapter discusses in more detail. Due to their agreement with prior expectations and to extract physical implications from the results, calculations without optical depth are treated as though they were valid in the subsequent paragraphs.

Examination of Figure 8 confirms that charm decays exceed pion and kaon contributions at earlier times. Peak flux values for $E_\nu = 10^9$ GeV are of similar magnitude, though pions experience stronger suppression from cooling when compared to kaons. Inclusion of secondary muons as indicated by [14] would lead to increased maxima, especially for neutrinos from pion decay, but does not significantly influence the relative peak positions. At lower energies, cooling factors approaching unity lead to pions becoming dominant, with kaons slightly below that. Neutrinos from charmed hadrons are now suppressed due to their lower production cross sections and branching ratios. The opposite behavior is seen as energies become larger, with contributions from charm dominating over those from pions and kaons. Light curves in Figure 8 are shaped by cooling factors at early times when all fluxes are suppressed, increase towards their maximum as decay and cooling timescales are equal, and subsequently decrease due to less protons being available. At later times, as E_p approaches E_h and hadron production is inhibited by energy conservation, a sharp cutoff is observed in the fluxes. These are universal characteristics, with charm, kaon and pion components being shifted with respect to each other as a result of their different masses and lifetimes. Besides changing their magnitudes, flux curves move towards earlier times at higher energies according to cooling and cutoff thresholds, with relative positions between individual contributions remaining mostly unaffected. The findings described so far are in agreement with results from [14].

4 Results

To evaluate the fluence, Figure 9 presents different time intervals, scaled by the squared neutrino energy. From the flux properties follows that charm decays dominate at earlier times, followed by kaons and pions. As the available proton energy reduces with time, each component contributes significantly at different energies, with neutrino fluence from charmed hadrons being the most energetic. Lower energies are found for kaons, while pions comprise the lowest energy part. Regarding magnitudes of the neutrino fluences, pion decay represents the largest contribution up to around $E_\nu = 10^8$ GeV energies, beyond which kaons begin to dominate. The fluence from charmed hadrons is relevant above $E_\nu = 10^9$ GeV as a threshold. Imposed by the maximum proton energy is $E_\nu = 10^{12}$ GeV as a hard cutoff, which is not visible in Figure 9 for improved readability. Contrary to what [14] shows, neutrinos from charm start decreasing closer to the kaon component, with kaons being approximately equal to the lower uncertainty bound for charmed hadrons at high energies. It is therefore unclear if a charmed neutrino component is unambiguously separable from pions and kaons. This discrepancy is at least partly attributable to the aforementioned larger maximum proton energy given in [14].

Continuing with results from an AGN accretion disk, there exists no temporal dimension, as the model assumes a constant neutrino spectrum at first approximation. Depicted in Figure 10 are the individual charmed hadron contributions to the total charm fluence, again with a scaling of neutrino energy squared. This agrees well with findings for the magnetar setting, as decays of both D^0 and D^+ dominate over D_s^+ and Λ_c^+ components at all energies. Thanks to its larger branching fraction, contribution from D^+ slightly exceeds D^0 up to $E_\nu = 10^9$ GeV despite having a smaller production cross section [46]. At higher energies, the longer lifetime for D^+ listed in Table 4 leads to suppression via cooling, leaving D^0 as the dominant charm contributor.

The combined charm fluence is presented by Figure 11 with neutrinos from pion and kaon decay. All curves have roughly similar shapes to those in Figure 9 for the magnetar scenario, with a slow rise at lower energies and a downward slope from cooling in higher energy ranges. The flat regions for pions and kaons are not visible in Figure 11 due to their longer lifetimes. Additionally, kaon decay surpasses the pion component at all included energies, though this changes towards lower energy values that are, however, excluded from the view in order to highlight charmed hadrons. Neutrino fluence from charm becomes dominant from around $E_\nu = 10^9$ GeV and starts to decrease above $E_\nu = 10^{10}$ GeV energies. This is consistent with expectations from cooling effects and sensitive to the chosen density, as larger values lead to a considerable reduction of the threshold energy. From its gradual slope up to the maximum charm fluence, one can infer a power law as the underlying proton spectrum, which is only slightly modified through the optical depth including a cross section (15) that slowly increases with energy. These results further account for decays occurring after hadrons have passed through the accretion disk by testing whether decay distances exceed the scale height and setting an according cooling factor, although no significant effects on the relative contributions are observed from including this additional step.

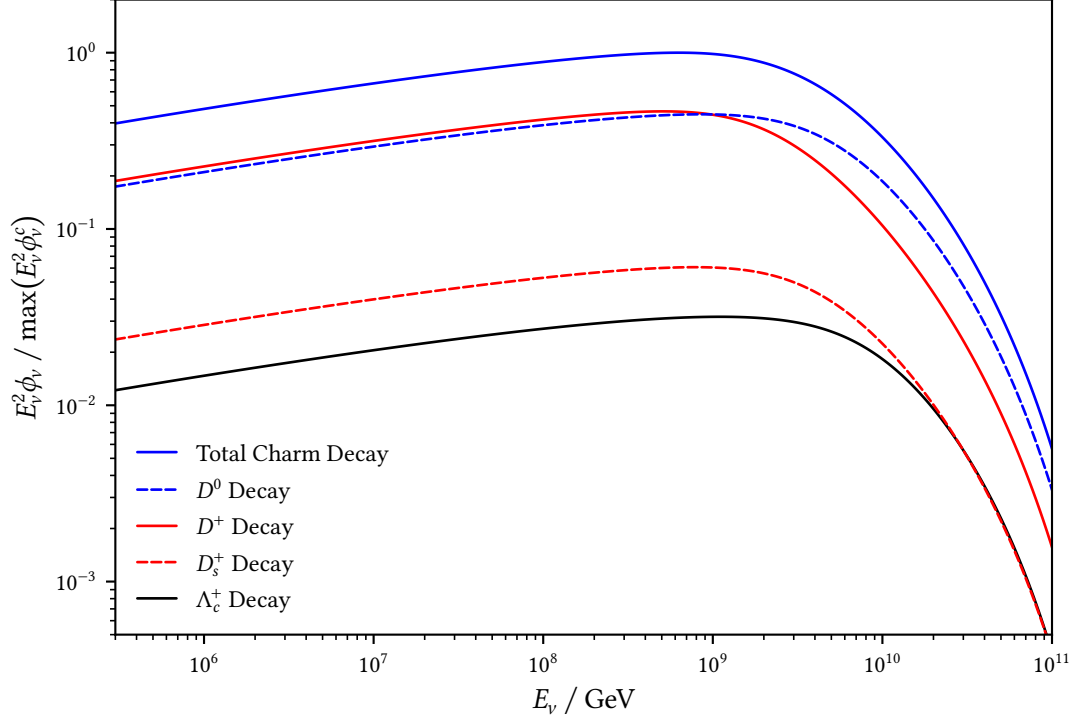


FIGURE 10: Comparison of individual charmed hadron contributions to the total charm neutrino fluence from an AGN accretion disk. Hadronic components similar to Figures 5 and 8 are found, where earlier times correspond to higher energies in these cases. Cooling becomes significant at lower energies for larger decay times, which leads to D^0 decreasing at a higher energy than D^+ decays, for example.

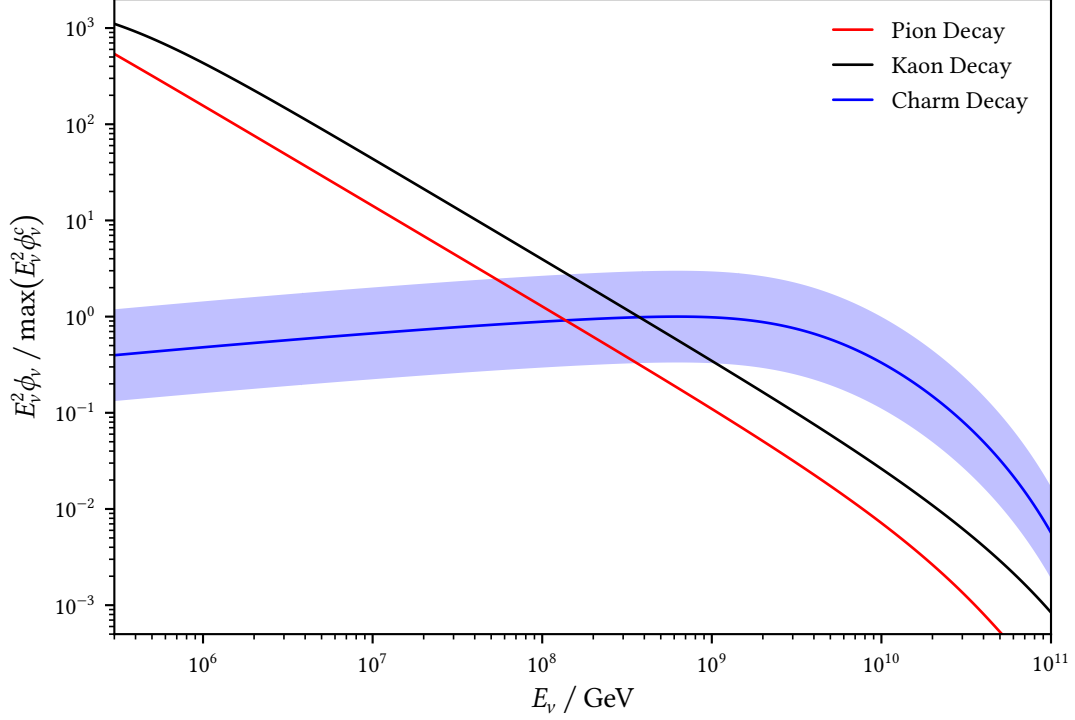


FIGURE 11: Expected neutrino fluence normalized to the maximum charmed hadron contribution from an AGN accretion disk. Differences between the shapes of pion and kaon components compared to charm decays result from the chosen view, as the flat increase observed for charmed hadrons occurs at lower energies in the case of pions and kaons due to their much longer lifetimes. These decay times are listed in Sections 3.1.1 and 3.2.1 with Figure 10 giving the reasoning for effects of cooling. Charmed hadrons dominate the fluence from $E_\nu = 10^9$ GeV and above, lining up with prior expectations. This threshold is sensitive to varying densities, with lower values producing a shift towards higher energies. A hard cutoff is enforced by $E_p = 10^{12}$ GeV as the maximum proton energy. The same shaded uncertainty band as in Figure 5 for charm decays as well as the scaling by E_ν^2 from Figure 6 are adopted.

5 Conclusion & Outlook

Throughout this thesis, models of astrophysical sources are developed to estimate the relative neutrino contribution from decays of charmed hadrons as well as pions and kaons. In order to do so, analytical parametrizations for cross sections as well as spectral distributions are taken from the literature and integrated numerically to obtain the desired results.

For the scenario of a young magnetar, a process following steps described in [14] is reproduced. Significant discrepancies are identified and determined to follow from including an effective optical depth. By omitting this coefficient, findings better match those presented in [14] except for a potentially erroneous maximum proton energy. Neutrinos from charm generally dominate at high energies or early times due to cooling factors suppressing longer lived pions and kaons. In the magnetar case, charmed hadron contributions are not clearly distinguishable from other components, which contradicts the clear separation observed in [14]. Natural extensions to this result are the inclusion of secondary muons as well as the calculation of a diffuse neutrino flux as in [14]. Potential improvements to the astrophysical modeling could be realized in terms of a more complex ejecta shell or by considering additional spindown mechanisms such as gravitational waves. The optical depth introducing major inconsistencies represents the most glaring issue for which no obvious solution is provided, and should therefore be investigated further, preferably by directly comparing to the explicit implementation used in [14]. This would also require replacing the parametrizations adopted for the present thesis with event generator results that are unfortunately inaccessible as well.

Transferring the approach to an AGN accretion disk setting produces results in line with prior expectations. At high energies, charm decays dominate the neutrino fluence and are cleanly separable from other contributions. This reflects the highly simplified model, which basically consists of a generic proton target with some astrophysical motivation behind it. Including synchrotron losses resulting from the presence of magnetic fields as well as the intense thermal radiation characteristic of AGN environments almost certainly affects the acquired results in a significant manner, potentially obscuring the accretion disk as a neutrino source altogether. Should this be the case, other source regions such as AGN jets might present more promising candidates for the evaluation of neutrinos from charm decays [38].

Overall, the contents of this thesis offer intriguing insights into the rich field of astroparticle physics and encourage deeper exploration of the broad range of relevant topics. Implemented methods are subject to additional optimizations, both in terms of more accurate parametrizations as well as better execution efficiency, although the procedures already are reasonably flexible, enabling future research by being able to easily adapt to more sophisticated models. Although the presented results are not fully conclusive, probing exotic decay processes via multimessenger neutrinos may well lead to novel discoveries in the study of energetic astrophysical processes.

Bibliography

- [1] P. Mészáros, D. B. Fox, C. Hanna, K. Murase, *Nature Reviews Physics* **1**, 585–599, ISSN: 2522-5820, DOI: [10.1038/s42254-019-0101-z](https://doi.org/10.1038/s42254-019-0101-z), arXiv: [1906.10212](https://arxiv.org/abs/1906.10212) [[astro-ph.HE](#)] (2019).
- [2] J. K. Becker, *Physics Reports* **458**, 173–246, ISSN: 0370-1573, DOI: [10.1016/j.physrep.2007.10.006](https://doi.org/10.1016/j.physrep.2007.10.006), arXiv: [0710.1557](https://arxiv.org/abs/0710.1557) [[astro-ph](#)] (2008).
- [3] A. A. Halim *et al.*, DOI: [10.48550/arXiv.2211.16020](https://doi.org/10.48550/arXiv.2211.16020), arXiv: [2211.16020](https://arxiv.org/abs/2211.16020) [[astro-ph.HE](#)] (2022).
- [4] A. M. Hillas, *Annual Review of Astronomy and Astrophysics* **22**, 425–444, DOI: [10.1146/annurev.aa.22.090184.002233](https://doi.org/10.1146/annurev.aa.22.090184.002233) (1984).
- [5] J. B. Tjus, L. Merten, DOI: [10.48550/arXiv.2002.00964](https://doi.org/10.48550/arXiv.2002.00964), arXiv: [2002.00964](https://arxiv.org/abs/2002.00964) [[astro-ph.HE](#)] (2020).
- [6] S. Gabici, C. Evoli, D. Gaggero, P. Lipari, P. Mertsch, E. Orlando, A. Strong, A. Vittino, *International Journal of Modern Physics D* **28**, 1930022, ISSN: 1793-6594, DOI: [10.1142/s0218271819300222](https://doi.org/10.1142/s0218271819300222), arXiv: [1903.11584](https://arxiv.org/abs/1903.11584) [[astro-ph.HE](#)] (2019).
- [7] L. O. Drury, *Astroparticle Physics* **39–40**, 52–60, ISSN: 0927-6505, DOI: [10.1016/j.astropartphys.2012.02.006](https://doi.org/10.1016/j.astropartphys.2012.02.006), arXiv: [1203.3681](https://arxiv.org/abs/1203.3681) [[astro-ph.HE](#)] (2012).
- [8] M. G. Aartsen *et al.*, *Science* **342**, 1242856, DOI: [10.1126/science.1242856](https://doi.org/10.1126/science.1242856), arXiv: [1311.5238](https://arxiv.org/abs/1311.5238) [[astro-ph.HE](#)] (2013).
- [9] M. G. Aartsen *et al.*, *The Astrophysical Journal* **833**, 3, ISSN: 1538-4357, DOI: [10.3847/0004-637x/833/1/3](https://doi.org/10.3847/0004-637x/833/1/3), arXiv: [1607.08006](https://arxiv.org/abs/1607.08006) [[astro-ph.HE](#)] (2016).
- [10] B. P. Abbott *et al.*, *Physical Review Letters* **116**, ISSN: 1079-7114, DOI: [10.1103/physrevlett.116.061102](https://doi.org/10.1103/physrevlett.116.061102), arXiv: [1602.03837](https://arxiv.org/abs/1602.03837) [[gr-qc](#)] (2016).
- [11] M. Aartsen *et al.*, *Science* **361**, ISSN: 1095-9203, DOI: [10.1126/science.aat1378](https://doi.org/10.1126/science.aat1378), arXiv: [1807.08816](https://arxiv.org/abs/1807.08816) [[astro-ph.HE](#)] (2018).
- [12] M. Aartsen *et al.*, *Science* **361**, 147–151, ISSN: 1095-9203, DOI: [10.1126/science.aat2890](https://doi.org/10.1126/science.aat2890), arXiv: [1807.08794](https://arxiv.org/abs/1807.08794) [[astro-ph.HE](#)] (2018).
- [13] K. Murase, P. Mészáros, B. Zhang, *Physical Review D* **79**, ISSN: 1550-2368, DOI: [10.1103/physrevd.79.103001](https://doi.org/10.1103/physrevd.79.103001), arXiv: [0904.2509](https://arxiv.org/abs/0904.2509) [[astro-ph.HE](#)] (2009).
- [14] J. A. Carpio, K. Murase, M. H. Reno, I. Sarcevic, A. Stasto, *Physical Review D* **102**, ISSN: 2470-0029, DOI: [10.1103/PhysRevD.102.103001](https://doi.org/10.1103/PhysRevD.102.103001), arXiv: [2007.07945](https://arxiv.org/abs/2007.07945) [[astro-ph.HE](#)] (2020).
- [15] J. Becker Tjus, W. Rhode, at European Physical Journal Web of Conferences, vol. 290, 10002, 10002, DOI: [10.1051/epjconf/202329010002](https://doi.org/10.1051/epjconf/202329010002).
- [16] M. E. Peskin, D. V. Schroeder, *An Introduction to Quantum Field Theory* (Westview Press, 1995), 866, ISBN: 9780429503559, DOI: [10.1201/9780429503559](https://doi.org/10.1201/9780429503559).
- [17] F. Halzen, A. Martin, *Quarks & Leptons: An introductory course in modern particle physics* (John Wiley & Sons, New York, USA, 1984), ISBN: 9780471887416.
- [18] N. Brambilla *et al.*, DOI: [10.48550/arXiv.hep-ph/0412158](https://doi.org/10.48550/arXiv.hep-ph/0412158), arXiv: [hep-ph/0412158](https://arxiv.org/abs/hep-ph/0412158) (2005).

Bibliography

- [19] P. D. Group *et al.*, *Progress of Theoretical and Experimental Physics* **2022**, 083C01, ISSN: 2050-3911, DOI: [10.1093/ptep/ptac097](https://doi.org/10.1093/ptep/ptac097) (2022).
- [20] T. K. Gaisser, R. Engel, E. Resconi, *Cosmic Rays and Particle Physics* (Cambridge University Press, Cambridge, Second Edition, 2016), ISBN: 9781139192194, DOI: [10.1017/CBO9781139192194](https://doi.org/10.1017/CBO9781139192194).
- [21] M. S. Longair, *High Energy Astrophysics* (Cambridge University Press, Cambridge, Third Edition, 2011), ISBN: 9780511778346, DOI: [10.1017/CBO9780511778346](https://doi.org/10.1017/CBO9780511778346).
- [22] A. Domínguez, J. D. Finke, F. Prada, J. R. Primack, F. S. Kitaura, B. Siana, D. Paneque, *The Astrophysical Journal* **770**, 77, ISSN: 1538-4357, DOI: [10.1088/0004-637x/770/1/77](https://doi.org/10.1088/0004-637x/770/1/77), arXiv: [1305.2162](https://arxiv.org/abs/1305.2162) [[astro-ph.CO](https://arxiv.org/archive/astro)] (2013).
- [23] C. Thompson, R. C. Duncan, *The Astrophysical Journal* **408**, 194, DOI: [10.1086/172580](https://doi.org/10.1086/172580) (1993).
- [24] B. Haskell, A. Sedrakian, in *Astrophysics and Space Science Library* (Springer International Publishing, 2018), Chapter 8, 401–454, ISBN: 9783319976167, ISSN: 2214-7985, arXiv: [1709.10340](https://arxiv.org/abs/1709.10340) [[astro-ph.HE](https://arxiv.org/archive/astro)].
- [25] Y. Sang, G. Chanmugam, *Astrophysical Journal* **363**, 597, DOI: [10.1086/169369](https://doi.org/10.1086/169369) (1990).
- [26] C. Alvarez, A. Carramiñana, *Astronomy & Astrophysics* **414**, 651–658, ISSN: 1432-0746, DOI: [10.1051/0004-6361:20031627](https://doi.org/10.1051/0004-6361:20031627), arXiv: [astro-ph/0311267](https://arxiv.org/abs/astro-ph/0311267) (2004).
- [27] A. J. Deutsch, *Annales d'Astrophysique* **18**, 1 (1955).
- [28] J. D. Jackson, *Classical Electrodynamics* (Wiley, New York, NY, Third Edition, 1999), ISBN: 9780471309321.
- [29] A. Gruzinov, *The Astrophysical Journal* **647**, L119–L122, ISSN: 1538-4357, DOI: [10.1086/506590](https://doi.org/10.1086/506590), arXiv: [astro-ph/0510751](https://arxiv.org/abs/astro-ph/0510751) (2006).
- [30] A. Spitkovsky, *The Astrophysical Journal* **648**, L51–L54, ISSN: 1538-4357, DOI: [10.1086/507518](https://doi.org/10.1086/507518), arXiv: [astro-ph/0603147](https://arxiv.org/abs/astro-ph/0603147) (2006).
- [31] P. Goldreich, W. H. Julian, *Astrophysical Journal* **157**, 869, DOI: [10.1086/150119](https://doi.org/10.1086/150119) (1969).
- [32] J. Li, A. Spitkovsky, A. Tchekhovskoy, *The Astrophysical Journal* **746**, 60, DOI: [10.1088/0004-637x/746/1/60](https://doi.org/10.1088/0004-637x/746/1/60), arXiv: [1107.0979](https://arxiv.org/abs/1107.0979) [[astro-ph.HE](https://arxiv.org/archive/astro)] (2012).
- [33] S. E. Gralla, N. Iqbal, *Physical Review D* **99**, ISSN: 2470-0029, DOI: [10.1103/physrevd.99.105004](https://doi.org/10.1103/physrevd.99.105004), arXiv: [1811.07438](https://arxiv.org/abs/1811.07438) [[hep-th](https://arxiv.org/archive/hep)] (2019).
- [34] M. Visser, DOI: [10.48550/arXiv.0706.0622](https://doi.org/10.48550/arXiv.0706.0622), arXiv: [0706.0622](https://arxiv.org/abs/0706.0622) [[gr-qc](https://arxiv.org/archive/gr)] (2008).
- [35] R. Blandford, D. Meier, A. Readhead, *Annual Review of Astronomy and Astrophysics* **57**, 467–509, ISSN: 1545-4282, DOI: [10.1146/annurev-astro-081817-051948](https://doi.org/10.1146/annurev-astro-081817-051948), arXiv: [1812.06025](https://arxiv.org/abs/1812.06025) [[astro-ph.HE](https://arxiv.org/archive/astro)] (2019).
- [36] M. A. Abramowicz, P. C. Fragile, *Living Reviews in Relativity* **16**, ISSN: 1433-8351, DOI: [10.12942/lrr-2013-1](https://doi.org/10.12942/lrr-2013-1), arXiv: [1104.5499](https://arxiv.org/abs/1104.5499) [[astro-ph.HE](https://arxiv.org/archive/astro)] (2013).
- [37] V. Beckmann, C. R. Shrader, DOI: [10.48550/arXiv.1302.1397](https://doi.org/10.48550/arXiv.1302.1397), arXiv: [1302.1397](https://arxiv.org/abs/1302.1397) [[astro-ph.HE](https://arxiv.org/archive/astro)] (2013).
- [38] K. Murase, F. W. Stecker, in *The Encyclopedia of Cosmology* (WORLD SCIENTIFIC, 2023), 483–540, ISBN: 9789811282645, DOI: [10.1142/9789811282645_0010](https://doi.org/10.1142/9789811282645_0010), arXiv: [2202.03381](https://arxiv.org/abs/2202.03381) [[astro-ph.HE](https://arxiv.org/archive/astro)].
- [39] B. Eichmann, F. Oikonomou, S. Salvatore, R.-J. Dettmar, J. B. Tjus, *The Astrophysical Journal* **939**, 43, ISSN: 1538-4357, DOI: [10.3847/1538-4357/ac9588](https://doi.org/10.3847/1538-4357/ac9588), arXiv: [2207.00102](https://arxiv.org/abs/2207.00102) [[astro-ph.HE](https://arxiv.org/archive/astro)] (2022).
- [40] V. Belousov, V. Ezhela, Y. Kuyanov, N. Tkachenko, *Physics of Atomic Nuclei* **79**, 113–117, DOI: [10.1134/S1063778816010075](https://doi.org/10.1134/S1063778816010075) (2016).
- [41] D. Fagundes, M. Menon, *Nuclear Physics A* **880**, 1–11, ISSN: 0375-9474, DOI: [10.1016/j.nuclphysa.2012.01.017](https://doi.org/10.1016/j.nuclphysa.2012.01.017), arXiv: [1112.5115](https://arxiv.org/abs/1112.5115) [[hep-ph](https://arxiv.org/archive/hep)] (2012).

Bibliography

- [42] D. A. Fagundes, M. J. Menon, P. V. R. G. Silva, *Journal of Physics G: Nuclear and Particle Physics* **40**, 065005, ISSN: 1361-6471, DOI: [10.1088/0954-3899/40/6/065005](https://doi.org/10.1088/0954-3899/40/6/065005), arXiv: [1208.3456](https://arxiv.org/abs/1208.3456) [hep-ph] (2013).
- [43] M. Froissart, *Phys. Rev.* **123**, 1053–1057, DOI: [10.1103/PhysRev.123.1053](https://doi.org/10.1103/PhysRev.123.1053) (3 1961).
- [44] V. P. Gonçalves, M. V. Machado, *Journal of High Energy Physics* **2007**, 028–028, ISSN: 1029-8479, DOI: [10.1088/1126-6708/2007/04/028](https://doi.org/10.1088/1126-6708/2007/04/028), arXiv: [hep-ph/0607125](https://arxiv.org/abs/hep-ph/0607125) (2007).
- [45] A. Bhattacharya, R. Enberg, M. H. Reno, I. Sarcevic, A. Stasto, *Journal of High Energy Physics* **2015**, ISSN: 1029-8479, DOI: [10.1007/jhep06\(2015\)110](https://doi.org/10.1007/jhep06(2015)110), arXiv: [1502.01076](https://arxiv.org/abs/1502.01076) [hep-ph] (2015).
- [46] R. Aaij *et al.*, *Journal of High Energy Physics* **2016**, [Erratum: JHEP 09, 013 (2016), Erratum: JHEP 05, 074 (2017)], 159, DOI: [10.1007/JHEP03\(2016\)159](https://doi.org/10.1007/JHEP03(2016)159), arXiv: [1510.01707](https://arxiv.org/abs/1510.01707) [hep-ex] (2016).
- [47] A. Metz, A. Vossen, *Progress in Particle and Nuclear Physics* **91**, 136–202, ISSN: 0146-6410, DOI: [10.1016/j.pnpnp.2016.08.003](https://doi.org/10.1016/j.pnpnp.2016.08.003), arXiv: [1607.02521](https://arxiv.org/abs/1607.02521) [hep-ex] (2016).
- [48] B. A. Kniehl, G. Kramer, *Physical Review D* **74**, ISSN: 1550-2368, DOI: [10.1103/physrevd.74.037502](https://doi.org/10.1103/physrevd.74.037502), arXiv: [hep-ph/0607306](https://arxiv.org/abs/hep-ph/0607306) (2006).
- [49] S. R. Kelner, F. A. Aharonian, V. V. Bugayov, *Phys. Rev. D* **74**, 034018, DOI: [10.1103/PhysRevD.74.034018](https://doi.org/10.1103/PhysRevD.74.034018), arXiv: [astro-ph/0606058](https://arxiv.org/abs/astro-ph/0606058) (3 2006).
- [50] A. Bhattacharya, R. Enberg, Y. S. Jeong, C. Kim, M. H. Reno, I. Sarcevic, A. Stasto, *Journal of High Energy Physics* **2016**, ISSN: 1029-8479, DOI: [10.1007/jhep11\(2016\)167](https://doi.org/10.1007/jhep11(2016)167), arXiv: [1607.00193](https://arxiv.org/abs/1607.00193) [hep-ph] (2016).
- [51] M. Lisovyi, A. Verbytskyi, O. Zenaiev, *The European Physical Journal C* **76**, ISSN: 1434-6052, DOI: [10.1140/epjc/s10052-016-4246-y](https://doi.org/10.1140/epjc/s10052-016-4246-y), arXiv: [1509.01061](https://arxiv.org/abs/1509.01061) [hep-ex] (2016).
- [52] E. V. Bugaev, A. Misaki, V. A. Naumov, T. S. Sinegovskaya, S. I. Sinegovsky, N. Takahashi, *Physical Review D* **58**, ISSN: 1089-4918, DOI: [10.1103/physrevd.58.054001](https://doi.org/10.1103/physrevd.58.054001), arXiv: [hep-ph/9803488](https://arxiv.org/abs/hep-ph/9803488) (1998).
- [53] R. S. Fletcher, T. K. Gaisser, P. Lipari, T. Stanev, *Phys. Rev. D* **50**, 5710–5731, DOI: [10.1103/PhysRevD.50.5710](https://doi.org/10.1103/PhysRevD.50.5710) (9 1994).
- [54] G. I. Lykasov, A. I. Malakhov, A. A. Zaitsev, *The European Physical Journal A* **57**, ISSN: 1434-601X, DOI: [10.1140/epja/s10050-021-00408-9](https://doi.org/10.1140/epja/s10050-021-00408-9), arXiv: [2012.02451](https://arxiv.org/abs/2012.02451) [hep-ph] (2021).
- [55] G. I. Lykasov, A. I. Malakhov, A. A. Zaitsev, *The European Physical Journal A* **58**, ISSN: 1434-601X, DOI: [10.1140/epja/s10050-022-00773-z](https://doi.org/10.1140/epja/s10050-022-00773-z), arXiv: [2201.10301](https://arxiv.org/abs/2201.10301) [hep-ph] (2022).
- [56] H. B. J. Koers, A. Pe’er, R. A. M. J. Wijers, arXiv: [hep-ph/0611219](https://arxiv.org/abs/hep-ph/0611219) (2006).
- [57] A. King, *New Astronomy Reviews* **52**, 253–256, DOI: [10.1016/j.newar.2008.06.006](https://doi.org/10.1016/j.newar.2008.06.006) (2008).
- [58] J. García, T. Dauser, C. S. Reynolds, T. R. Kallman, J. E. McClintock, J. Wilms, W. Eikmann, *The Astrophysical Journal* **768**, 146, ISSN: 1538-4357, DOI: [10.1088/0004-637x/768/2/146](https://doi.org/10.1088/0004-637x/768/2/146), arXiv: [1303.2112](https://arxiv.org/abs/1303.2112) [astro-ph.HE] (2013).
- [59] J. García, T. Dauser, A. Lohfink, T. R. Kallman, J. F. Steiner, J. E. McClintock, L. Brenneman, J. Wilms, W. Eikmann, C. S. Reynolds, F. Tombesi, *The Astrophysical Journal* **782**, 76, ISSN: 1538-4357, DOI: [10.1088/0004-637x/782/2/76](https://doi.org/10.1088/0004-637x/782/2/76), arXiv: [1312.3231](https://arxiv.org/abs/1312.3231) [astro-ph.HE] (2014).
- [60] P. Haensel, J. P. Lasota, J. L. Zdunik, DOI: [10.48550/arXiv.astro-ph/9901118](https://doi.org/10.48550/arXiv.astro-ph/9901118), arXiv: [astro-ph/9901118](https://arxiv.org/abs/astro-ph/9901118) (1999).